INFORMATION TO USERS

This manuscript has been reproduced from the microfilm master. UMI films the text directly from the original or copy submitted. Thus, some thesis and dissertation copies are in typewriter face, while others may be from any type of computer printer.

The quality of this reproduction is dependent upon the quality of the copy submitted. Broken or indistinct print, colored or poor quality illustrations and photographs, print bleedthrough, substandard margins, and improper alignment can adversely affect reproduction.

In the unlikely event that the author did not send UMI a complete manuscript and there are missing pages, these will be noted. Also, if unauthorized copyright material had to be removed, a note will indicate the deletion.

Oversize materials (e.g., maps, drawings, charts) are reproduced by sectioning the original, beginning at the upper left-hand corner and continuing from left to right in equal sections with small overlaps. Each original is also photographed in one exposure and is included in reduced form at the back of the book.

Photographs included in the original manuscript have been reproduced xerographically in this copy. Higher quality 6" x 9" black and white photographic prints are available for any photographs or illustrations appearing in this copy for an additional charge. Contact UMI directly to order.

UMI

A Bell & Howell Information Company
300 North Zeeb Road, Ann Arbor MI 48106-1346 USA
313/761-4700 800/521-0600

Université d'Ottawa · University of Ottawa

Vortex Localization in single crystals of $Tl_2Ba_2CuO_{6+\delta}$ with columnar defects: an empirical model.

by

Daniel S.M. Cameron

Thesis submitted to the University of Ottawa
in partial fulfillment of the requirements
for the degree of Master of Science in Physics

Department of Physics
University of Ottawa, Ottawa, Canada
June, 1997

0-612-26306-1

Acknowledgements

I am sincerely grateful and most certainly indebted to my research supervisor Dr. Marcel LeBlanc for his time spent and patience granted in guiding me through the many topics we have pursued in reaching this ultimate goal, especially when assistance was most needed.

I wish to express my gratitude to my parents who brought me up and provided me with the opportunity to complete my education without great financial burden.

I would also like to thank David LeBlanc for many interesting conversations as well as his help in our many collaborations.

Finally I dedicate this thesis to my girlfriend Natalie for her love and support throughout this project and also to our future together.

Foreword

During the summer of 1994, before I registered in the M.Sc. program, I participated in an experimental project in Dr. Julian Cave's group at the Institut de Recherche d'Hydro-Quebec as part of the ongoing collaboration of this group and Dr. M. LeBlanc in the study of AC losses in high temperature superconductors. My contribution is acknowledged as a co-author of a report in the conference proceedings[1].

Since Sept. 1994 as an M.Sc. candidate I have pursued a variety of research activities under the direction of Dr. LeBlanc which I now enumerate.

First I carried out some measurements on the thermal disclosure of hidden magnetic moments. This work was undertaken to familiarize me with the experimental techniques, instruments, sample and magnet assemblies, data acquisition procedures, etc., exploited in the investigations of critical current and magnetic behaviour in type II superconductors pursued in Dr. LeBlanc's lab.

As an initiation to the analysis of magnetic and critical current phenomena in type II superconductors I assisted in the development of a model accounting for the observation on the thermal release of hidden magnetic moments in very hysteretic type II superconductors. A preliminary report[2] was presented at the CAP Congress, June 1995.

In collaboration with David LeBlanc and under the direction of Dr. LeBlanc I assisted in the development of a generalized empirical model describing the hysteretic behaviour of the critical current in weak-linked granular high T_c superconductors. This phenomenon has been observed and qualitatively explained by many researchers. A preliminary report[3] was presented at the CAP Congress, June 1995.

Many workers have reported on the observation of a large increase in the diamagnetic magnetic moment of weak-linked granular high T_C superconductors upon slow warming after fast and slow cooling. Under the direction of Dr. LeBlanc I pursued calculations for a simple empirical model which quantitatively accounts for these observations. A preliminary report[4] was presented at the CAP Congress, June 1995.

I completed a theoretical analysis of the effect of the flux density configuration on the magnetic relaxation rate in type II superconductors which had been undertaken by S. Celebi, a Ph.D. candidate in our lab. Jean-Philippe Pascal, a summer student in our group, also participated in this project. A manuscript reporting on this work has been submitted for publication in Cryogenics[5].

In collaboration with David LeBlanc and Martin Krzywinski, a summer student, I made an important contribution to an empirical theoretical study of magnetic relaxation along bridges between the envelopes of the major hysteresis loops in type II superconductors. A manuscript reporting on these calculations has been accepted for publication in Superconductor Science and Technology[6].

I played a major role in the development of a model which predicts an appreciable reduction of low frequency AC losses in coaxial cables of type II superconductors by a steady bias current. This work was published in the Journal of Applied Physics[7] in January 1996. A reprint is appended to this thesis.

Again in collaboration with David LeBlanc and under the direction of Dr. LeBlanc I played a major role in the development of an empirical model which accounts for a variety of observations of a University of Chicago and Argonne National Laboratory collaboration on the local magnetic relaxation and hysteresis in single crystals of a high T_C superconductor ($YBa_2Cu_3O_{7-x}$) with columnar defects. This work appeared as a Rapid Communication[8] in the March 1 issue of Physical Review B. A reprint is appended to this thesis.

In this thesis I only present my most recent research project. This work was entirely carried by me under the direction of Dr. LeBlanc and has been jointly submitted for publication[9] in Physical Review B1.

Reports and Publications

1. Dag Willen, Raphael Nadi, Dan Cameron, Benoit Turcotte, Wen Zhu, Michel Trudeau and Julian Cave, 1st Superconductivity Workshop, 1994.
2. M.A.R. LeBlanc, Dan Cameron, David LeBlanc and Selahattin Celebi, "Thermal Release of Hidden Magnetic Moments in Hysteretic Type II Superconductors." CAP Congress, June 1995.
3. M.A.R. LeBlanc, David LeBlanc and Dan Cameron, "I_C Hysteresis in Granular Type II Superconductors: A Simple Model." CAP Congress, June 1995.
4. M.A.R. LeBlanc and Daniel Cameron, "Evolution of the Magnetic Moment in Granular High T_C Superconductors upon Fast and Slow Cooling and Warming." CAP Congress, June 1995.
5. M.A.R. LeBlanc, Daniel S.M. Cameron, Selahattin Celebi and Jean-Philippe Pascal, "Effect of the flux density configuration on the magnetic relaxation rate in type II superconductors." Submitted to Cryogenics, 1997.

6. M.A.R. LeBlanc, Daniel S.M. Cameron, Martin Krzywinski and David LeBlanc, “Magnetic Relaxation on Bridges between the Envelopes of Major Hysteresis Loops of Type II Superconductors.” Accepted for publication in Superconductor Science and Technology, 1997.
7. M.A.R. LeBlanc, Daniel S.M. Cameron, David LeBlanc and Jinglei Meng, J. Appl. Phys. 79, 334 (1996).
8. M.A.R. LeBlanc, Daniel S.M. Cameron and David LeBlanc, Phys. Rev. B55, R6141 (1997).
9. M.A.R. LeBlanc and Daniel S.M. Cameron “Vortex localization in single crystals of $Tl_2Ba_2CuO_{6+\delta}$ with columnar defects: an empirical model.” Submitted to Physical Review B1, May 1997.

Abstract

The peaks and valleys observed by Nowak et al (Phys. Rev. B54, R12725 (1996)) in the local magnetization $M(x)$ and local relaxation rate $S(x)$ in a single crystal of $Tl_2Ba_2CuO_{6+\delta}$ containing columnar defects are well reproduced by an empirical model where the critical current density j_C is fractionally enhanced in the vicinity of the matching field B_ϕ and of a multiple of B_ϕ by superimposing two broad triangular peaks on a continuous dependence of j_C on the magnetic flux density B. The dependence of $S(x)$ on $B(x)$ is well reproduced by stipulating that j_C decays at a rate $\approx 1/2$ slower at the summit of the peaks than at their edges. The model fits the variety of $M(x)$ and $S(x)$ data taking B_{S1} and B_{S2}, the flux density at the first and second peaks in j_C, to have a ratio $B_{S2} / B_{S1} \approx 2.5$. The model also makes detailed predictions regarding the structure and location of valleys for $S(x)$ versus $B(x)$ descending in magnitude which were not reported in the above article.

We demonstrate that a "staircase" type of dependence of j_C on B proposed by Radzihovsky (Phys. Rev. Letters 74, 4923 (1995)) and exploited by Beauchamp et al (Phys. Rev. B52, 13025 (1995)) can account for the peak in $|M(x)|$ adjacent to B = 0 but cannot generate the two peaks encountered when $B(x)$ is ascending in magnitude nor reproduce the two peaks seen at higher fields when $B(x)$ is descending in magnitude.

We also show that the ratio $B_{V2\uparrow} / B_{V1\uparrow} \approx 3$ for the location of the two valleys observed for $S(x)$ versus $B(x)$ depends on, (i) the position of the

measuring probes and, (ii) whether $B(x)$ is ascending or descending in magnitude.

Table of Contents

Chapter 1

General Introduction

General Background

An important property of superconductors is clearly their ability to support a transport current with no energy dissipation.[1-5] In type I superconductors this capacity abruptly ceases when the total magnetic field at the surface of the conductor attains the thermodynamic critical field H_C. This distressing feature was first observed by Kamerlingh Onnes soon after his discovery of superconductivity in 1911. Since the highest $\mu_0 H_C \approx 0.07$ Tesla in type I superconductors is encountered in Pb at $T \approx 0\,\mathrm{K}$, these materials have not been particularly useful in this area of applications. When $|\vec{H}_{total}|$, the vector sum of externally applied magnetic fields and the "self" field generated by the current in the superconductor attains H_C, an intermediate state arises where zones of normal material of thickness $\approx \lambda \approx 100$ nm, the penetration depth, coexist alongside superconducting regions of comparable size. Under these circumstances some electrical resistance appears.

Although many type II superconductors such as classical low T_C materials (e.g. Nb, NbTi and Nb_3Sn) and high T_C superconductors possess an H_C much larger than Pb, when the total surface field exceeds $H_{C1} \approx \frac{H_C}{\sqrt{2}(\lambda/\xi)} \ln\left(\frac{\lambda}{\xi}\right)$ which is intrinsically much smaller than H_C, a mixed state occurs. Here ξ is the coherence length and typically $\xi << \lambda$. In this mixed state, magnetic flux in the form of quantized vortices, also called flux lines, enters the bulk of the specimen. In "ideal", i.e. reversible hence pinning free specimens, these flux lines move freely and form a uniform triangular lattice. Since parallel flux lines repel each other, this lattice adopts a homogeneous density whose equilibrium is maintained by the "magnetic pressure" of the external magnetic field H_a.

It is useful here to focus on the simple geometry of a long ribbon where H_a is directed along the broad faces and transverse to the length of the ribbon. In this situation it is clear that the introduction of a conduction current along the length of the ribbon will disturb the equilibrium of the flux line lattice. The magnetic field H_I generated by the electric current enhances the surface field along the face where $H_{total} = H_1 = H_a + H_I$ and diminishes H_{total} along the opposite face since here $H_{total} = H_2 = H_a - H_I$. Consequently a gradient of magnetic flux density arises across the width of the ribbon. Thus each flux line experiences a stronger mutual repulsion from the flux lines on its high-density side than it experiences from those on its low-density side. The unbalance experienced by the flux lines will cause them to move "down" the flux density gradient. In the steady state, hence with a constant (D.C.) current flowing, new flux lines enter across the surface where $H_{total} = H_1$ and "old" lines leave at the same rate across the surface where $H_{total} = H_2$. The displacement of a flux line however gives rise to energy dissipation since Cooper pairs are thereby driven to traverse the normal core of the moving flux line. A voltage V_f, denoted a flux flow voltage, then appears along the length of the ribbon hence a flux flow resistance $R_f = V_f / I$

and energy dissipation $P_f = IV_f$. Alternatively and equivalently, the driving force on the flux lines when an electric current and the associated magnetic field are introduced in the body or bulk of the specimen can be viewed as the Lorentz force $\bar{F}_L = \bar{j} \times \bar{B}$ where $\bar{j}$ is the current density.

In brief then, when the total magnetic field, $H_a + H_I$ at one surface of the ribbon attains H_{C1}, the reversible, hence pinning free, type II superconductor ceases to carry an electric current with zero resistance. Consequently "ideal" type II superconductors are even less interesting than type I materials for applications which require large electric currents and strong magnetic fields. Reversible (i.e. high purity and well annealed) Nb is an exceptional case since here $\mu_0 H_C \approx 0.18\,\mathrm{T}$ and $\mu_0 H_{C1} \approx 0.12\,\mathrm{T}$ are appreciably larger than $\mu_0 H_C \approx 0.07\,\mathrm{T}$ for Pb at 0°K. Also since $T_C \approx 9\,\mathrm{K}$, this metal is very useful for superconducting high internal electric and magnetic field microwave applications (such as klystrons for nuclear particle accelerators).

Unfortunately then, for "ideal" (i.e. reversible, hence pinning free) type II superconductors, whether low or high T_C, the immense span between H_{C1} and the upper critical field, $H_{C2} = \sqrt{2}\lambda H_C/\xi$, although academically fascinating, is barren for practical purposes.

Hysteretic Type II Superconductors

In the early sixties this situation changed overnight when a group at Bell Laboratories discovered that Nb_3Sn, a brittle alloy with a $T_C \approx 18\,\mathrm{K}$, could sustain large currents in the presence of strong magnetic field as high as 10 Tesla at 4.2 K. Soon after this breakthrough, R. Hake and T.G. Berlincourt found that ductile NbTi alloys with a $T_C \approx 11$ K could, when "suitably prepared", support large currents at 4.2 K in fields extending to several Teslas. The latter alloy has since been the "workhorse" material exploited in the construction of thousands of laboratory (e.g. the Tevatron at Fermi Lab) and commercial (Magnetic Resonance Imaging) superconducting magnets. These alloys can carry such large currents in the mixed state (also called the vortex state and the Shubnikov phase) between H_{C1} and H_{C2} because here the flux lines cannot move freely but are "pinned" by suitable imperfections and impurities, which impede or arrest their migration.

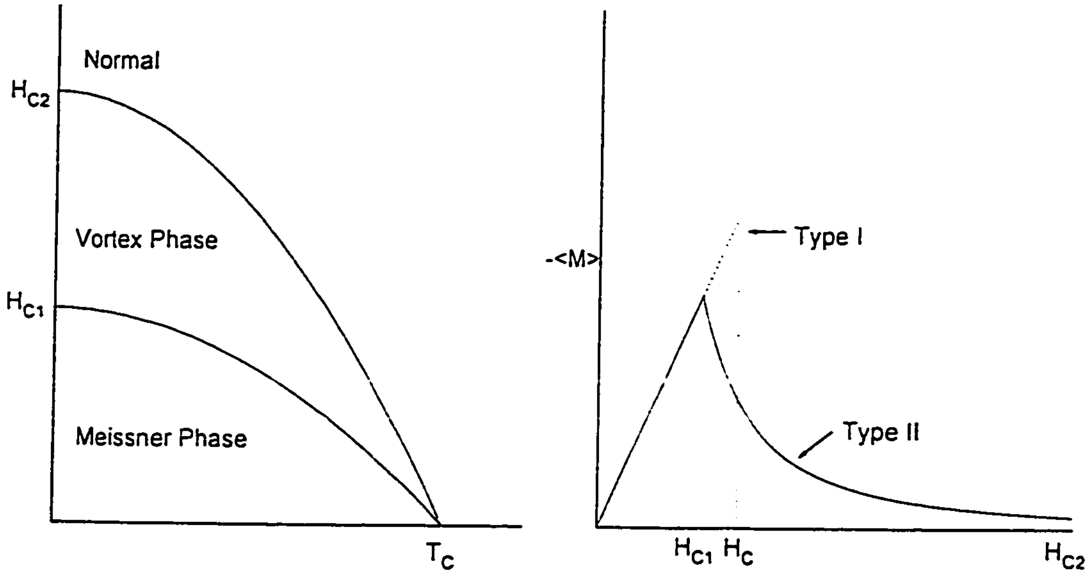

Now a large net repulsive force can be exerted on a flux line by its neighbours before it is released from the pinning sites. Thus large density gradients dB/dx can be established in the distribution of flux lines, hence large lossless current densities can be sustained since $|dB/dx| = \mu_0 j$ by Maxwell's equation. Alternatively the driving Lorentz force $\bar{F}_L = \bar{j} \times \bar{B}$ now must overcome a pinning force $\bar{F}_P$ before migration of the flux lines takes place.

This leads to the concept of the critical state where $|\bar{F}_L| = |\bar{j} \times \bar{B}|$ must infinitesimally exceed $|\bar{F}_P|$ in any volume which becomes occupied by an electric current, hence by a flux density gradient. Returning again to the simple geometry of a long wide ribbon in a static magnetic field H_a directed along a broad face and perpendicular to its length, we can readily envisage a sequence of critical flux density configurations (called B profiles) penetrating into the specimen as sketched in Fig. 1.1(a) when a current I is introduced, hence as the self-field H_I increases to $+I/2$ along one surface and "decreases" to $-I/2$ along the other surface of the specimen. Here I denotes the current flowing through a unit dimension of the width (height) of the ribbon. In the sketch we visualize that the specimen is first cooled from T_C to the chosen temperature T_F in $H_a >> H_{C1}$, hence the initial B profile is uniform with $B(x) = \mu_0 H_a$. This is referred to as field cooling.

When I reaches the critical current, I_C, the entire specimen is filled by the current at a critical current density j_C, hence by a critical flux density gradient. We note that j_C may depend on the flux density $B(x)$, hence $j_C(x)$ and dB/dx are not uniform since $B(x)$ is not uniform. When I is made to exceed I_C, $j(x)$ becomes greater than $j_C(x)$ and $|\bar{F}_L| > |\bar{F}_P|$ throughout the volume of the ribbon. Now a uniform electric field, $E = B(x)\,\mathrm{v}(x)$, hence a flux flow voltage appears accompanied by energy dissipation, $P = VI$, as a continuous procession of flux lines enters from the surface on the right, travels at a velocity $\mathrm{v}(x)$ across the width of the ribbon and exits through the left surface. Critical current densities $j_C \approx 10^{11}$ A/m^2 have been achieved in

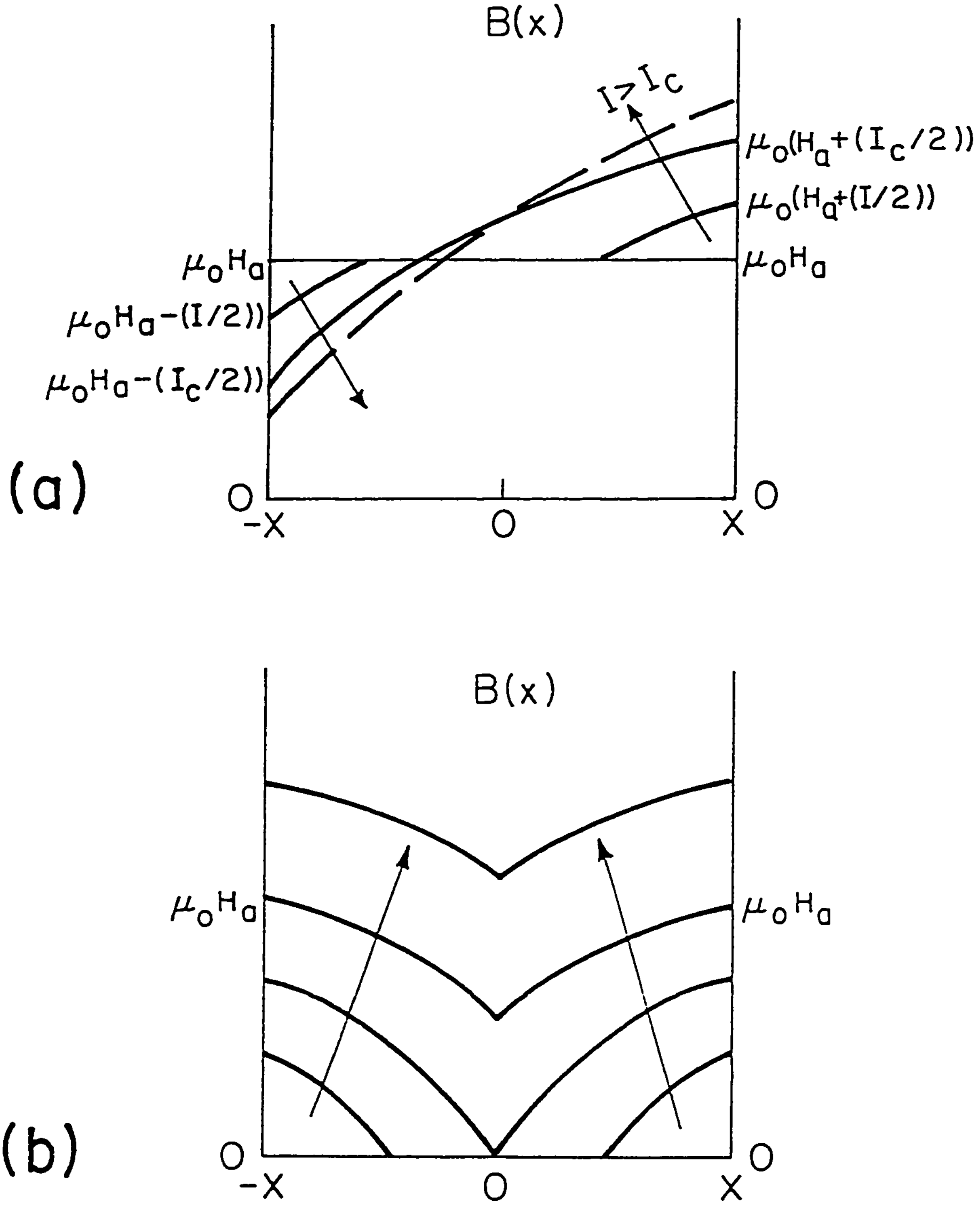

Fig. 1.1 (a) Sequences of B profiles with I increasing in static H_a.
(b) Sequences of B profiles with H_a increasing with $I = 0$.

the “best” low and high T_C materials in applied magnetic fields of several Teslas.

Another simple scenario of great interest is the situation where only the externally applied magnetic field H_a plays a role and no conduction current is fed into the ribbon via leads attached to its ends. These are the circumstances which will be addressed in this thesis. Sequences of B profiles are displayed in Fig. 1.1(b). Here a non-uniform electric field $E(x) = B(x)\mathrm{v}(x)$ is generated as flux lines enter and migrate in the specimen during the “transition” from one stationary B profile to the subsequent one. During the interval of evolution of the B profiles, $j(x) > j_C(x)$ and $|\bar{F}_L| > |\bar{F}_P|$.

Fig. 1.2 displays a sequence of B profiles which are generated when the applied field H_a after attaining a very large value, denoted $H_{\max}$, is now slowly reduced to zero and then increased in magnitude in the opposite direction. The reader will note that the lower half of Fig. 1.2 repeats Fig. 1.1(b) but with the sign reversed. Physically however these two sets of configurations are similar.

Since the profiles are symmetric with respect to the centre of the specimen when $I = 0$, I will henceforth simplify these pictures and present only the left part of the sequences of profiles in the displays in the thesis.

In the experimental work addressed in this thesis, the researchers measured the evolution of the flux density $B(x)$ threading a small area of thin platelet single crystals with a miniature Hall probe as the applied magnetic field directed perpendicular to the flat faces of the specimen was slowly varied from a large value in one direction, through zero, then to a large value in the opposite direction.

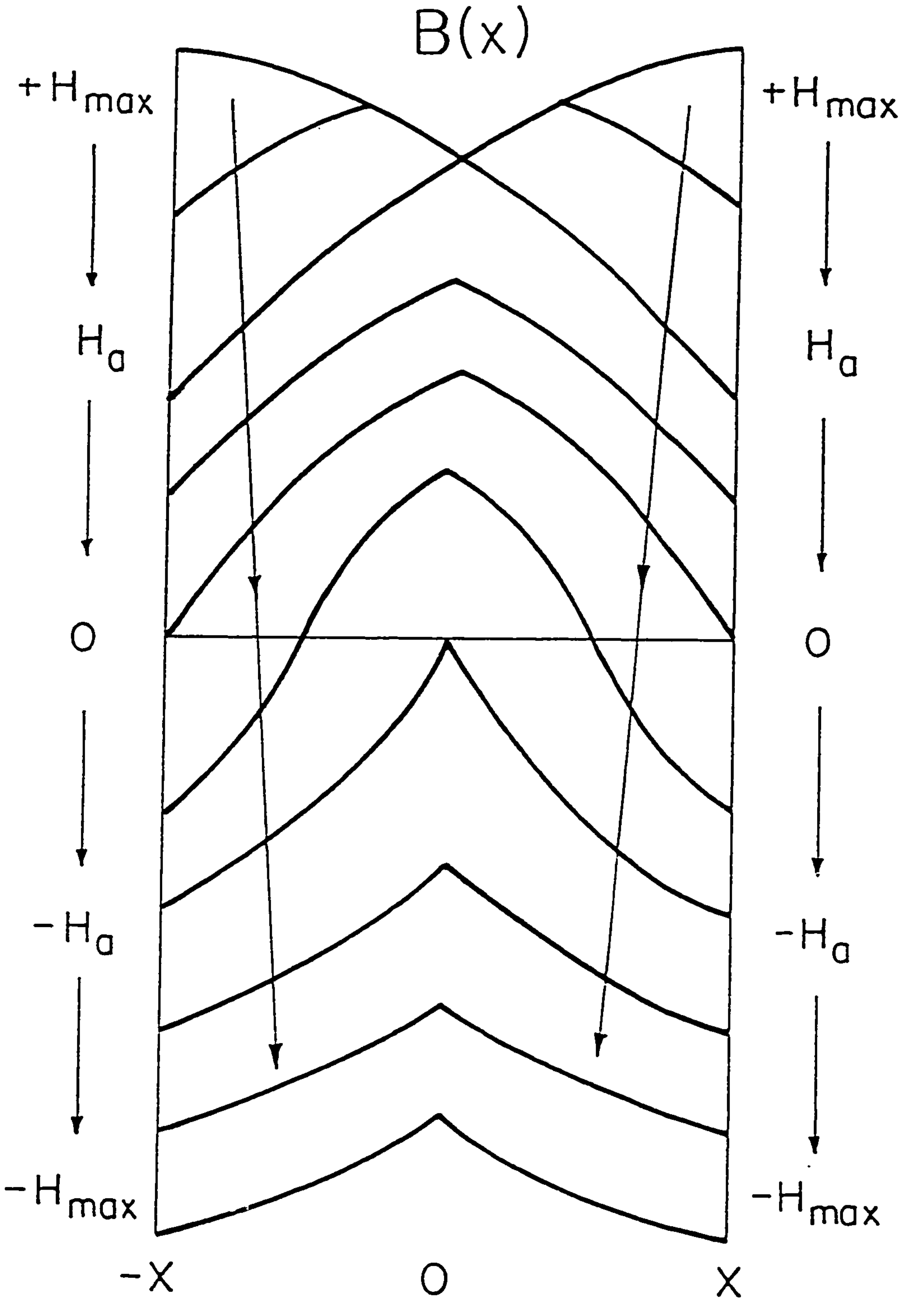

Fig. 1.2 A sequence of B profiles generated as H_a, after attaining a strength H_{max}, is then reduced, traverses zero and increases in magnitude in the opposite direction. Note that now a swing of H_a from $-H_{max}$ to $+H_{max}$ will simply "repeat" this sequence.

It is useful to display the observations in various formats which I now describe. Firstly the evolution of $B(x)$ versus $\mu_0 H_a$ can be presented in the straightforward manner sketched in Fig. 1.3(a). This is recognized as the standard textbook illustration of hysteresis curves for ferromagnets. This format however fails to focus on and emphasize the important quantity under scrutiny which is the difference between $\mu_0 H_a$ and $B(x)$, namely the local magnetization, $\mu_0 M(x) = B(x) - \mu_0 H_a$. Fig. 1.3(b) schematically presents typical hysteresis curves in this second format. Workers have also found it convenient to modify this second format and to display $\mu_0 M(x)$ versus $B(x)$ instead of $\mu_0 H_a$. A typical hysteresis curve encountered in this format is sketched in Fig. 1.3(c). Note in particular the changes of quadrant between (b) and (c) for the hump or peak.

Often the measurement of the evolution of $B(x)$ during the variation of H_a, after a reversal of the sense of sweep, which causes $M(x)$ or $B(x)$ to migrate from the lower (upper) to the upper (lower) envelopes of these hysteresis curves are not shown since these "bridges" or "traversals" are not pertinent to the message being reported and take place outside the boundaries selected for the display. Note also that the information contained in quadrant 1 of all these figures is repeated in quadrant 3 and that of quadrant 2 in 4. Consequently all of these formats could "economically" be reduced to a display of either the right or left half without a loss of information.

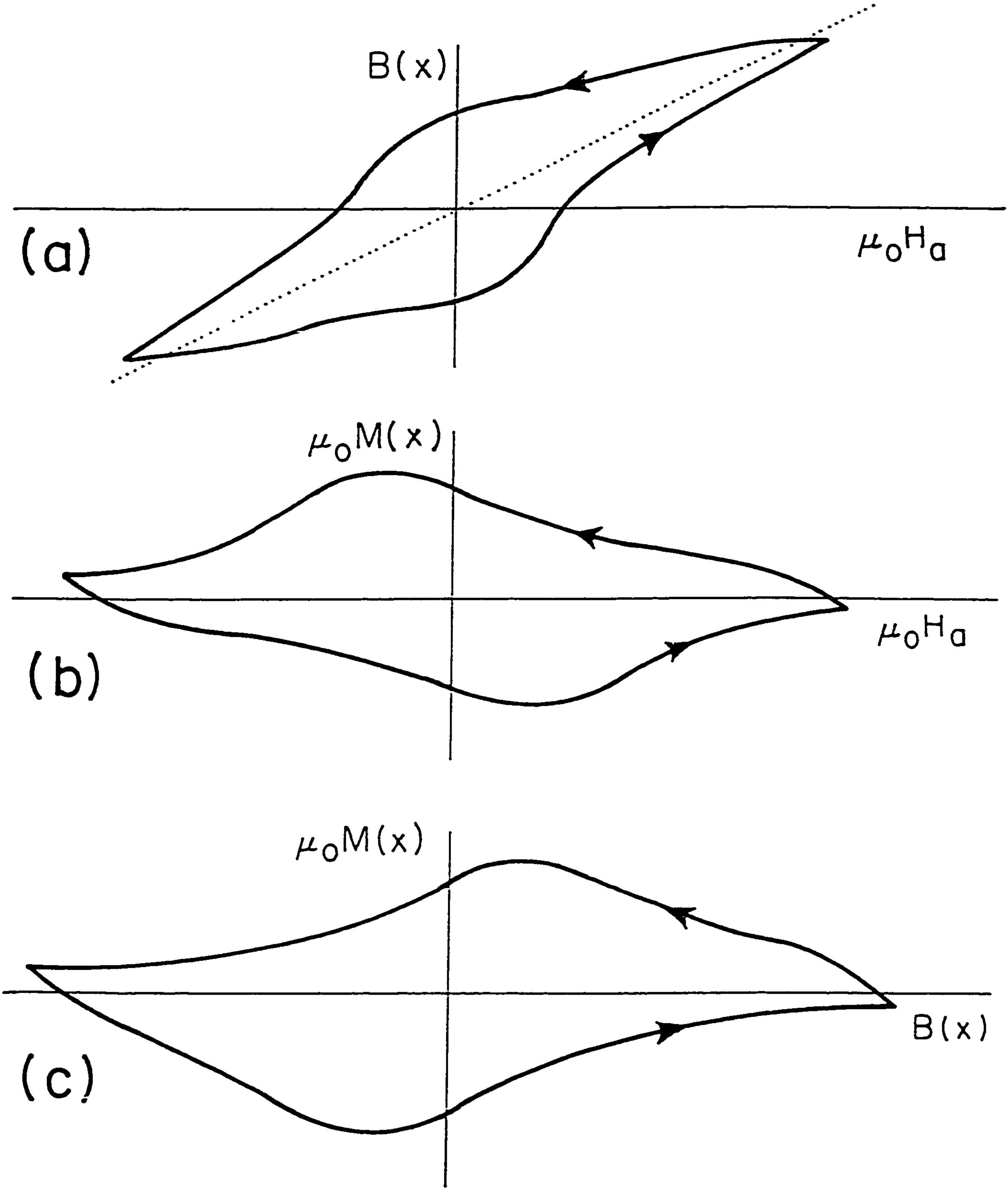

Fig. 1.3 Three different formats for the presentation of local hysteresis curves.

An Elementary Outline of the Physics of Pinning

It is well established that magnetic flux in the body of type II superconductors exists in the form of quantized vortices each threaded by one unit of flux, $\Phi_O = h/2e = 2.05$ (10^{-15}) T•m^2. Theoretical and experimental investigations of the internal structure of the vortices reveal that the density of Cooper pairs hence the superconducting state (energy gap, order parameter) diminish to zero at the axis of the vortex. This reduction or suppression of the superconductivity occurs over a characteristic dimension denoted ξ and called the coherence length. In high T_C superconductors and the well known low T_C type II superconductors (NbTi, Nb_3Sn) $\xi << \lambda$ and typically ξ is a few nanometers in the T = 0 limit. Both ξ and λ diminish with temperature and become infinitely large at T_C.

A useful and frequently exploited approximation is to regard the area $\pi\xi^2$ around the axis of the vortex to be in the normal state. Hence this region is denoted the vortex core. Independently of this simple picture, it is clear that superconducting condensation energy, $V_{core} \approx n_s \pi \xi^2 L$, must be sacrificed when a vortex "appears" in the superconductor. Here n_s is the density of Cooper pairs in the unperturbed superconducting state, hence far from the vortex cores. L is the length of the vortex. Consequently, the energy advantage associated with the "nucleation" of the vortex is partly offset by the creation of the vortex core. It ensues that voids and other regions in the body of the superconductor where the density of Cooper pairs is already suppressed or reduced over a volume of $\approx \xi^3$ will provide excellent sites to be exploited in placing the axis of the vortex since the energy ransom has

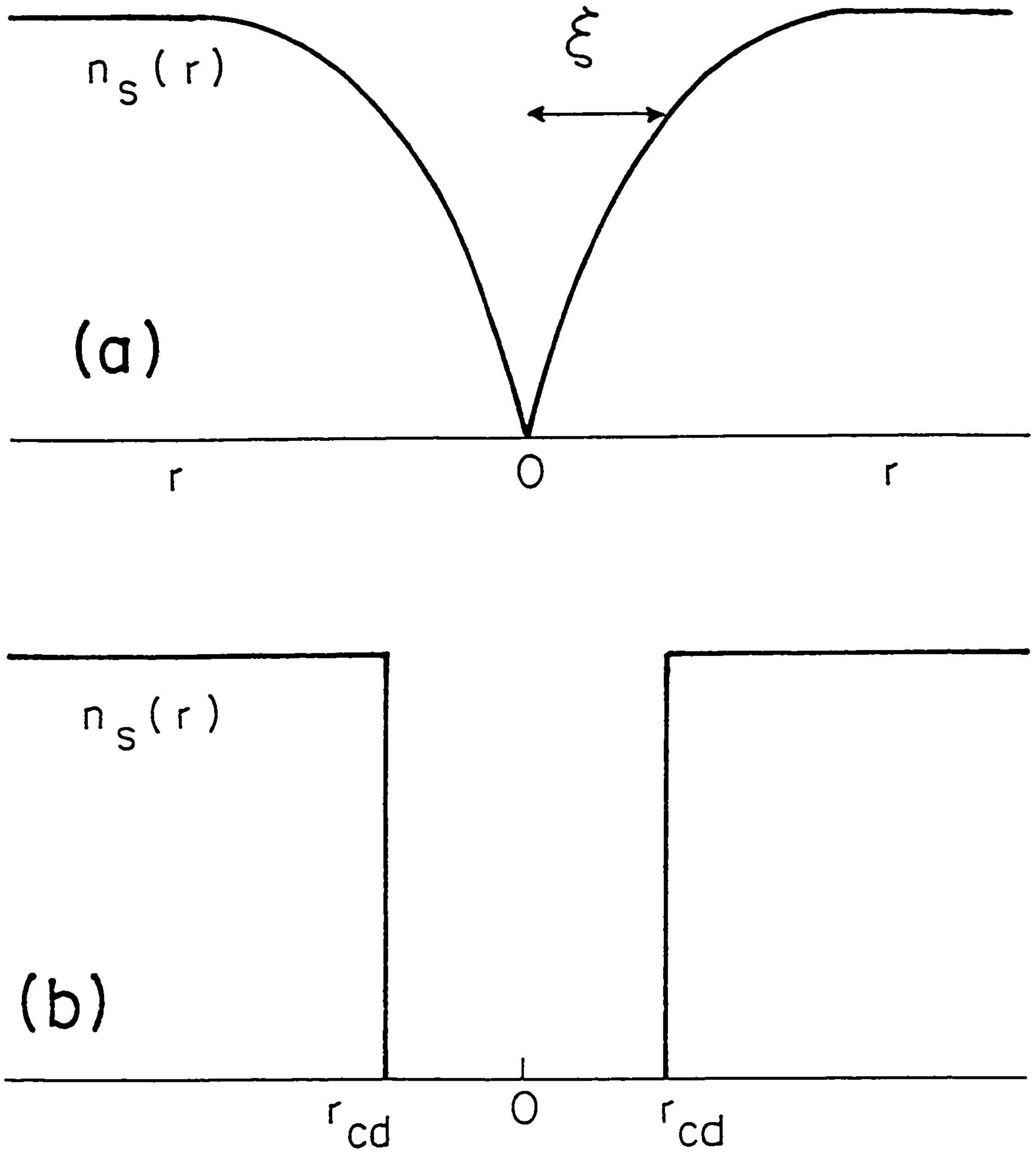

Fig. 1.4 (a) The density of Cooper pairs in the vicinity of a vortex core.
(b) A columnar defect of volume $\approx \xi^2 L$, where L is the length of the defect.

already been paid. Thus the vortex (flux lines) will seek to occupy the available physical imperfections and regions of chemical impurities of appropriate dimensions, orientation and distribution as depicted in Fig. 1.4. The energy gain for the vortex in occupying these sites must then be supplied in order that the flux line be liberated and made to migrate. The lattice of flux lines is thereby pinned by a force density F_P which the Lorentz force $|\bar{F}_L| = |\bar{j} \times \bar{B}|$ must overcome before the flux flow state occurs and energy dissipation appears.

The microstructure of type II superconductors therefore plays the major role in dictating the critical current density, $j_C(B,T)$ of these materials. For more than three decades teams of metallurgists, materials scientists, physicists and chemists have investigated the effectiveness of different "point defects", grain boundaries, dislocation networks, precipitates, microsegregation of phases, etc., in order to optimize and understand the pinning phenomenon. As part of this effort many laboratories have studied the effect of bombarding the specimens with high energy protons, alpha particles, fast neutrons, X-rays, etc. Recently several laboratories have irradiated small single crystals of high T_C superconductors with high energy heavy ion beams. Such a beam directed to traverse a single crystal platelet along its thickness (typically $\approx$a dozen microns) creates an irregular lattice of columnar defects extending from one surface to the other. The size of the ions and their energy determine the diameter of these columnar defects. The choice of these is made to create columnar defects whose radius corresponds to the coherence length of the target over some convenient temperature range ΔT below T_C. In this thesis I first present the hysteretic behaviour of single crystals of $Tl_2Ba_2CuO_{6+\delta}$ containing columnar defects reported recently by a University of Chicago and Argonne National Laboratory group and then examine these observations in the framework of the critical state model mentioned above and which I now outline in more detail.

The Critical State Model

This model, as indicated earlier, assumes that flux lines are made to migrate when the driving Lorentz force overcomes the pinning force. An alternative perspective focuses on the feature that the flux lines depin and migrate only when the current density exceeds a critical value $j_C(B(x),T)$. Then Maxwell's equation for planar geometry reads,

$$dB/dx = \pm\mu_O j_C(B,T) \qquad \textbf{(1.1)}$$

with $F_p(B,T) = j_C(B,T)B$.

Many workers in the early sixties, starting with C.P. Bean, H. London, Y.B. Kim and P.W. Anderson, noted that various simple expressions for $j_C(B)$ readily lead to a satisfactory description of a large variety of observations on the critical current behaviour, low frequency AC losses and magnetic phenomena in type II superconductors. In particular expressions of the form,

$$j_c = j_O B_{ref}^n / (B_O + B)^n \qquad \textbf{(1.2)}$$

have been extensively exploited in the literature. Here j_O, B_O and n characterize the specimen and j_O is dominant in prescribing the temperature dependence. For situations where B extends to $\mu_O H_{C2}$, this expression is modified to take into account that $j_C \to 0$ when $B \to \mu_O H_{C2}$. It is this empirical approach which we apply in our examination of the observations of the Chicago/Argonne group in order to extract information on $j_C(B)$ for their single crystals with columnar defects.

These workers observe new features of basic significance in the local hysteresis curves, namely peaks in $|M(x)|$ versus $B(x)$ whose maxima appear in the vicinity of $B(x) = B_\phi$ and a multiple of B_ϕ. Here B_ϕ denotes the matching field where the density of flux lines, $N_f = B(x)/\Phi_O = N_{cd}$, where N_{cd} is the density of columnar defects. Recall that $\Phi_O = h/2e$ is the quantum of flux.

Flux Creep

In 1962, Kim, Hempstead and Strnad at Bell Labs observed that the magnetic field H_i in the cavity of a hollow tube of Nb_3Sn at 4.2 K in a stationary external magnetic field H_a directed along its axis changed slowly with time. This indicated that the current I circulating azimuthally around the tube was not truly persistent but experienced some decay. In these experiments the workers insured that ΔH_a, the previous increase or decrease of H_a which induced the flux shielding or flux retaining current I to circulate around the tube, was sufficiently large so that I existed in a critical state, i.e. filled the entire wall thickness.

An explanation of this remarkable phenomenon, called flux creep, was proposed by P.W. Anderson in 1962. The basic elements of this model survive in the numerous subsequent and very elaborate theoretical studies of this phenomenon. Prior to the discovery of high T_C superconductors, this behaviour was not disturbing and did not attract much attention since the rate of decay was infinitesimal and was observed to diminish logarithmically with time.

Soon after the discovery of high T_C superconductors it was found that in these materials the rate of decay is immense not only at 77 K but also at 4.2 K. The phenomenon was then baptised "giant flux creep". Also in these materials the rate of decay frequently deviates appreciably from the usual logarithmic dependence with time.

P.W. Anderson believed that thermal agitation caused individual flux lines or bundles of flux lines to escape from the pinning potential wells of depth U (also called the activation energy or barrier) with a probability $e^{-U/kT}$. When the B profile is uniform, the rate of escape of flux lines from potential wells is balanced over an appropriate time interval and spatial extent by the rate of capture by potential wells. However, a flux density gradient created by an electric current lowers the barrier on one side of a potential well by an amount ΔU and raises the barrier on the other side by an equal amount as illustrated here in the sketch. Thus the escape probabilities are altered, increasing by an amount $e^{+\Delta U/kT}$ on the low flux density side and decreasing by $e^{-\Delta U/kT}$ on the high side. This results in a thermal agitation

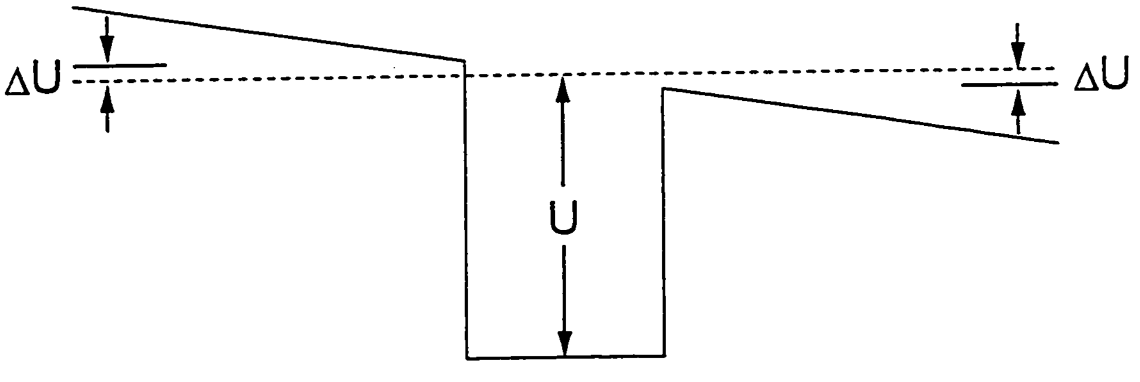

driven net movement of flux lines "down" the flux density gradients, hence a "relaxation" of the B profiles, therefore a decline in the steepness of the flux density gradient, and consequent decay of the current density j. As these related events take place, the rate of flux creep (also called magnetic relaxation) diminishes since the decrease of j "causes" dB/dx to also diminish hence ΔU to become smaller. ΔU depends on j, B and T. Further the prefactor to the exponential involves much physics. Extensive experimental and theoretical effort has been and is being devoted to elucidating these many features and, in particular, the effect of different pinning sites on the rate of flux creep.

The giant flux creep encountered at low temperatures in the high T_C superconductors is partly attributed to the feature that the coherence length in these materials is very small (typically $\xi \approx 1$ nm) and hence the pinning potential wells are less effective than in their low T_C counterparts where ξ is much larger.

It is of course not necessary to use hollow tubes for the investigations of flux creep. This is usually done by monitoring the evolution with time of the magnetic moment of a specimen of arbitrary geometry at constant temperature and in a stationary magnetic field (this is another reason why flux creep is also labelled magnetic relaxation). In order to compare "apples with apples" it is customary to normalize $\Delta\mu/\Delta t$, the rate of decay of the magnetic moment with respect to the initial magnetic moment μ, hence display $\Delta\mu/\mu\Delta t$ versus t or $\ln t$.

The Chicago/Argonne group measured the rate of relaxation of the local magnetic flux density, hence $dB(x)/dt$, as a function of $B(x)$ ascending in magnitude at one position on their single crystal with columnar defects.

These measurements were performed at 0.5 and 2 K. They observe nearly identical intricate structure as a function of $B(x)$ with sharp minima in the normalized decay rate, $dB(x)/dt|M(x)|$ occurring in the vicinity of B_ϕ and 3 B_ϕ at both temperatures.

In chapter 4 of this thesis, by introducing two simple new assumptions, we reproduce these intricate observations using the same critical state framework which we exploited to generate all the details in the structure of their local hysteresis curves. Crucial features which emerge from our model are that the position of the minima depends on, (i) the location of the probe measuring $B(x)$ and (ii) whether $B(x)$ is ascending or descending in magnitude. In our model, the important physical quantity is the location of the maxima of two peaks in the dependence of j_C on B. Our analysis of their data shows that these are situated in the vicinity of B_ϕ and 2.5 B_ϕ. Consequently the 3 B_ϕ feature which they emphasize arises from their choice for the position of the probe and the fact that they focused only on relaxation data taken with $B(x)$ increasing in magnitude.

Chapter 2

Experimental Observations

In this chapter I present the experimental observations of a University of Chicago/Argonne National Lab group (Nowak et al[6]) which our empirical model endeavours to reproduce and analyze.

First, as a preface, it is of interest to mention a similar investigation on single crystals of $YBa_2Cu_3O_{7-x}$ with columnar defects by other University of Chicago/Argonne National Lab collaborations[7,8] both published a year earlier.

The crystals in the latter studies were polygon shaped platelets, at least 150×150 μm in area in the a-b plane and less than 20 μm thick. The columnar defects were introduced along the c-axis by irradiation with 605 MeV Xe ions and extend from face to face of the crystal.

Fig 2.1 presents their data on the effect of the irradiation on the local hysteresis curve, $B(x)$ versus $\mu_0 H_a$ at 0.1 K. Here the Hall probe of active area 5 μm × 10 μm was situated at the centre of one face of the specimen. The notation $B_\phi = 0$ indicates no irradiation and $B_\phi = 10$ and 20 kG indicates that the irradiation was monitored to achieve a density of columnar defects to match the density of flux lines threading the platelet along the c-axis when the magnetic flux density $B(x)$ has the value indicated.

Pursuing the critical state concept outlined in the introduction and developed in the appendix, and assuming that the irradiation simply modifies the parameters j_0 and B_0 in the expression,

$$j_C = \frac{j_O B_{ref}}{B_O + B} \qquad \textbf{(2.1)}$$

LeBlanc, Cameron and LeBlanc[9] generated the corresponding family of curves displayed in Fig. 2.2(a).

Fig. 2.3(a) displays the observations of the third University of Chicago/Argonne collaboration (Beauchamp et al[8]) of the local hysteresis curves for different positions of the measuring probe between the middle and the outside edge. The measurements were performed on the crystal irradiated to $B_\phi = 10$ kG (see the thicker curve of Fig 2.1) but here $T = 5$ K instead of 0.1 K.

Fig 2.3(b) displays the theoretical curves generated by the model proposed by Beauchamp et al[8] to account for the dependence of the hysteresis curve on the position of the probe. The model is based on the concept put forward by one of their theoreticians (Radzihovsky[10]) that j_C should decrease very rapidly when B is increased across B_ϕ. Fig 2.2(b) displays the corresponding family of curves generated by our model which assumes j_C to be continuous (see inset to Fig 2.2(a) and equation 2.1).

Briefly then the U. of Chicago/Argonne group (Beauchamp[8]) and ourselves[9] interpret the same data in radically different ways. We assume that the irradiation causes a continuous change in j_C versus B with no discontinuity across B_ϕ whereas they maintain that the irradiation introduces a large enhancement in j_C (by a factor of $\approx$ 8) below B_ϕ with a steep descent in the vicinity of B_ϕ.

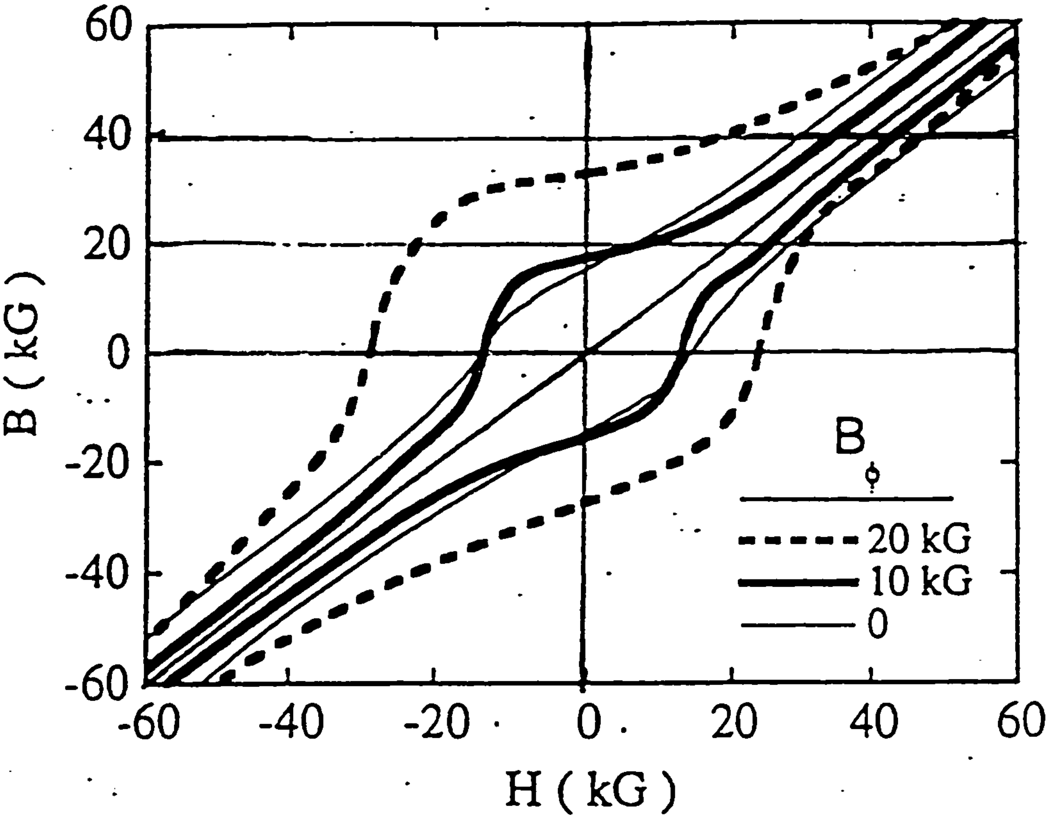

FIG. 1. Hysteresis loops at $T = 0.1$ K for crystals with no columnar defects and with columnar defect densities equivalent to the vortex density at internal magnetic fields $B_\phi = 10$ and 20 kG. The sharp changes in slope scale with B_ϕ.

Fig. 2.1 Reproduced from Beauchamp et al[2]

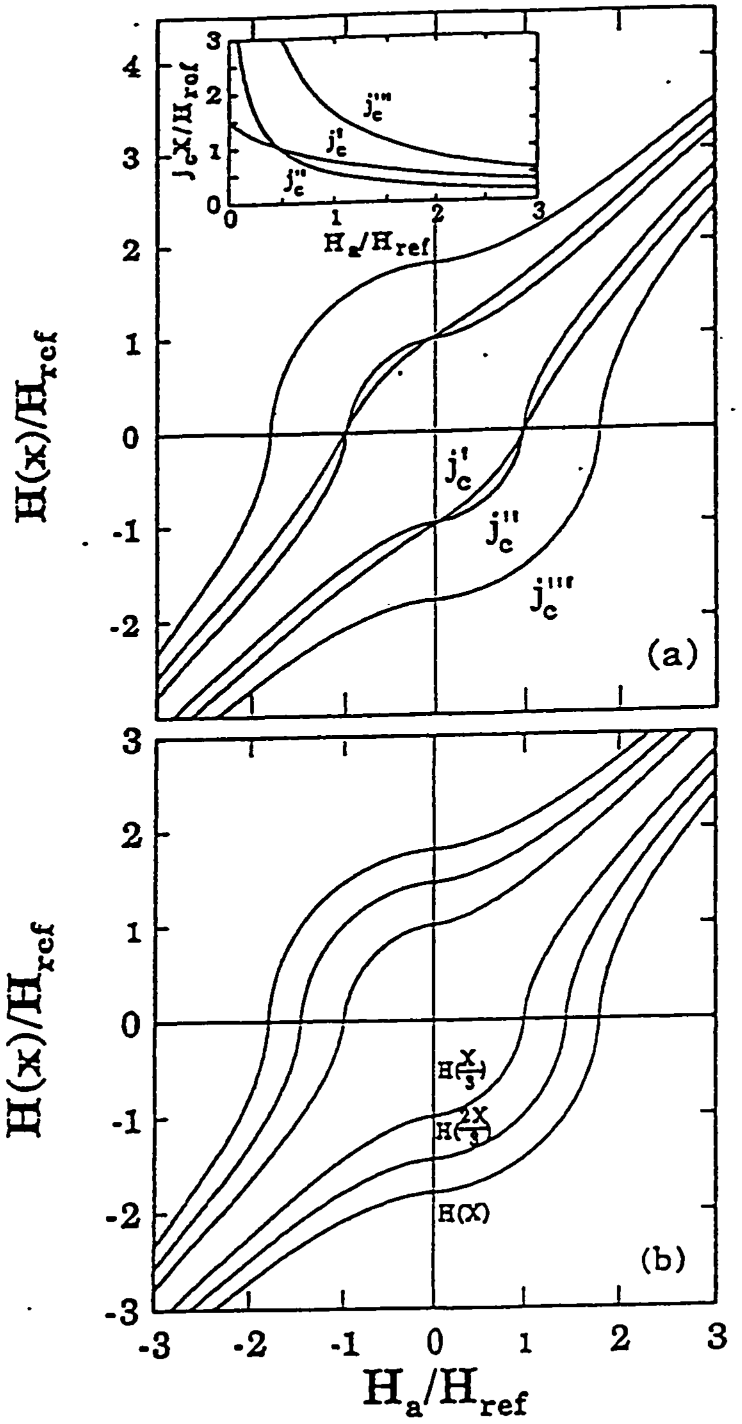

Fig. 2.2 Reproduced from LeBlanc et al[4]

FIG. 2. (a) Displays hysteresis curves of $H(x)$, the magnetic field at the center of the specimen vs H_a, the applied magnetic field, calculated using $j_c = j_0 H_{\rm ref}/[H(x)+H_0]$ shown in the inset with $j_0X/H_{\rm ref} = 1.5$, 0.6, and 1.8, and $H_0/H_{\rm ref} = 1.0$, 0.12, and 0.10 for $j_c = j_c'$, j_c'', and j_c'''. Taking $\mu_0 H_{\rm ref} \approx 1.5$ T gives a good fit to Fig. 1 of Ref. 2. (b) Displays local hysteresis curves $H(x)$ for different distances from the surface ($x/X = 1/3$, 2/3, and 1 for the inner, middle, and outer curves) calculated using j_c'''.

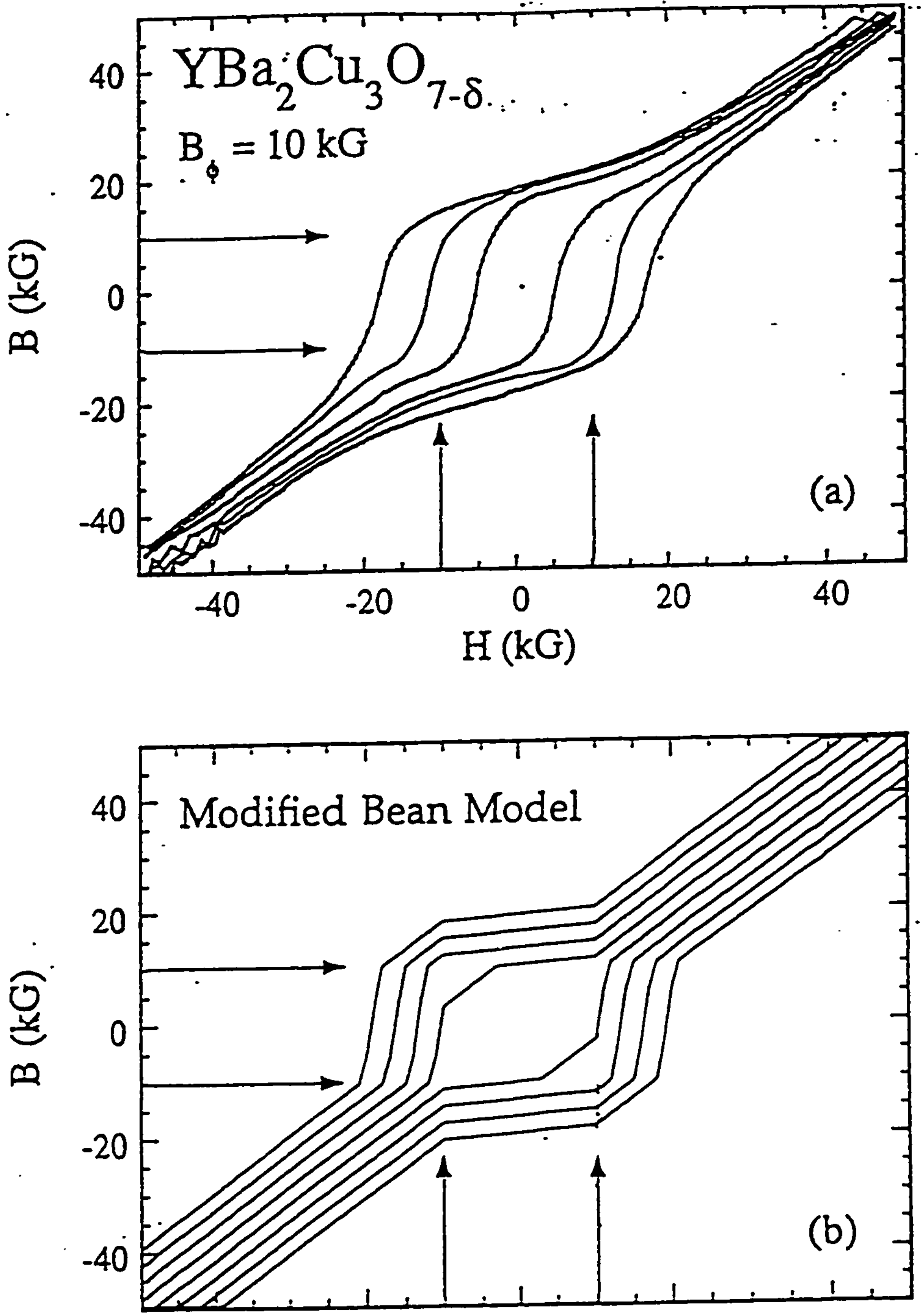

FIG. 1. (a) Local internal magnetic field B vs applied field H at 25 μm (inner curve), 50 μm, and 70 μm (outer curve) distances from the crystal edge at $T = 5$ K. (b) Calculated local hysteresis loops using modified Bean model with $B_\phi = 10$ kG.

Fig. 2.3 Reproduced from Beauchamp et al[3]

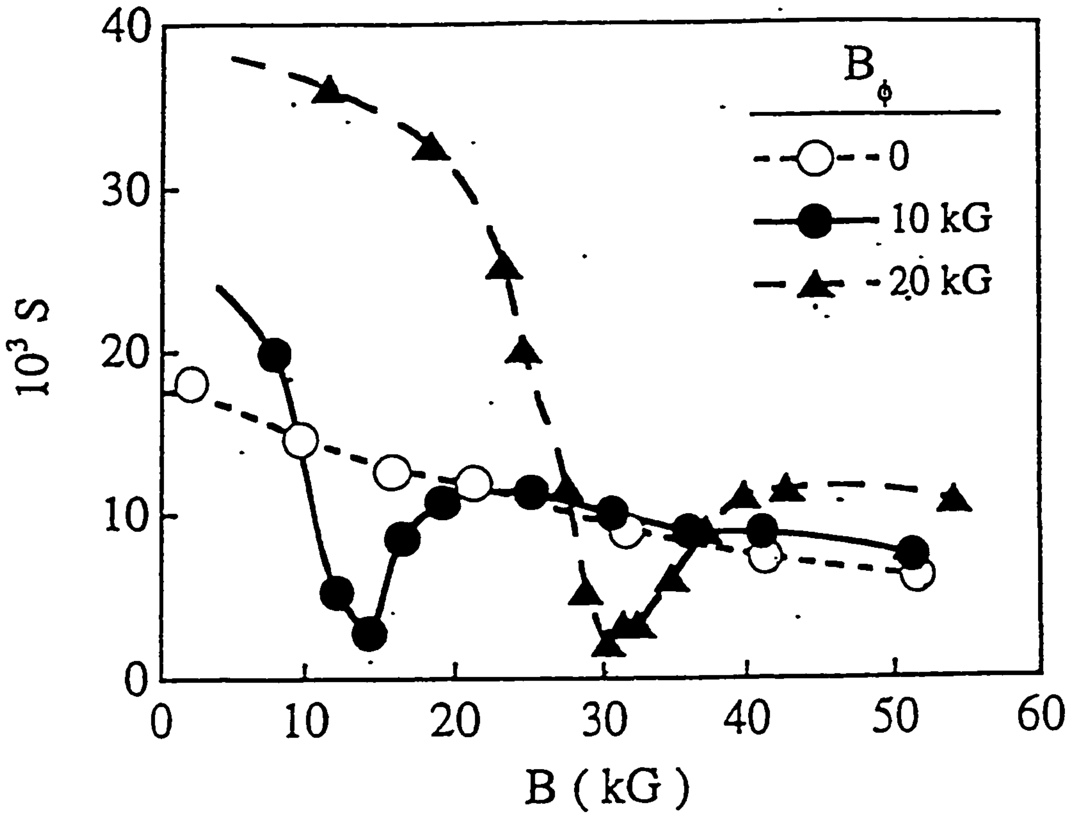

FIG. 3. Scaling of the minimum in the magnetization relaxation rate with columnar defect density at $T = 0.1$ K. Th crystal with no columnar defects has no features in $S(B$ whereas the crystals with $B_\phi = 10$ and 20 kG have large enhancements in S for $B < B_\phi$, a sharp minimum near B_ϕ, an an approach to the point defect pinning limit for $B \gg B_\phi$ Lines are guides to the eye.

Fig. 2.4 Reproduced from Beauchamp et al[2]

The observations of Beauchamp et al[7] on the effect of the levels of ion irradiation, hence of the density of columnar defects on the local magnetic relaxation (flux creep) are displayed in Fig 2.4. Here the decay rate is plotted versus $B(x)$ with the Hall probe placed at the middle of the platelet crystal of Fig 2.1. Note the appearance of a deep valley in the irradiated samples where the minima are linked to B_ϕ, and the growth in B_ϕ caused by doubling the density of columnar defects.

Finally we now turn to the observations of Nowak et al[6] on the effect of columnar defects created by high energy heavy ions in single crystals of $Tl_2Ba_2CuO_{6+\delta}$. The superconducting and normal state properties of this material exhibit considerably more anisotropy between the basal a-b plane and the c-axis than $YBa_2Cu_3O_{7-x}$ The single crystals were irregularly shaped platelets with basal plane areas approximately 200 × 200 μm and 20 μm thick along the c-axis. The randomly distributed columnar defects were aligned along the axis ($\pm 2°$) and were introduced by irradiating one of the crystals with 1.1 GeV uranium ions. The irradiation dosage was chosen so that the density of defects corresponded to vortex densities at a matching field $B_\phi = 10$ kG.

The magnetization measurements were performed using microfabricated bismuth Gaussmeters similar to those used by Beauchamp et al[7,8] except that the active area of the probe was 3 μm × 3 μm. The magnetic field was detected by monitoring the Hall voltage. The probe was placed on the surface at $x/X = 2/3$ where $x = 0$ is the edge of the platelet and $x = X$ is the middle.

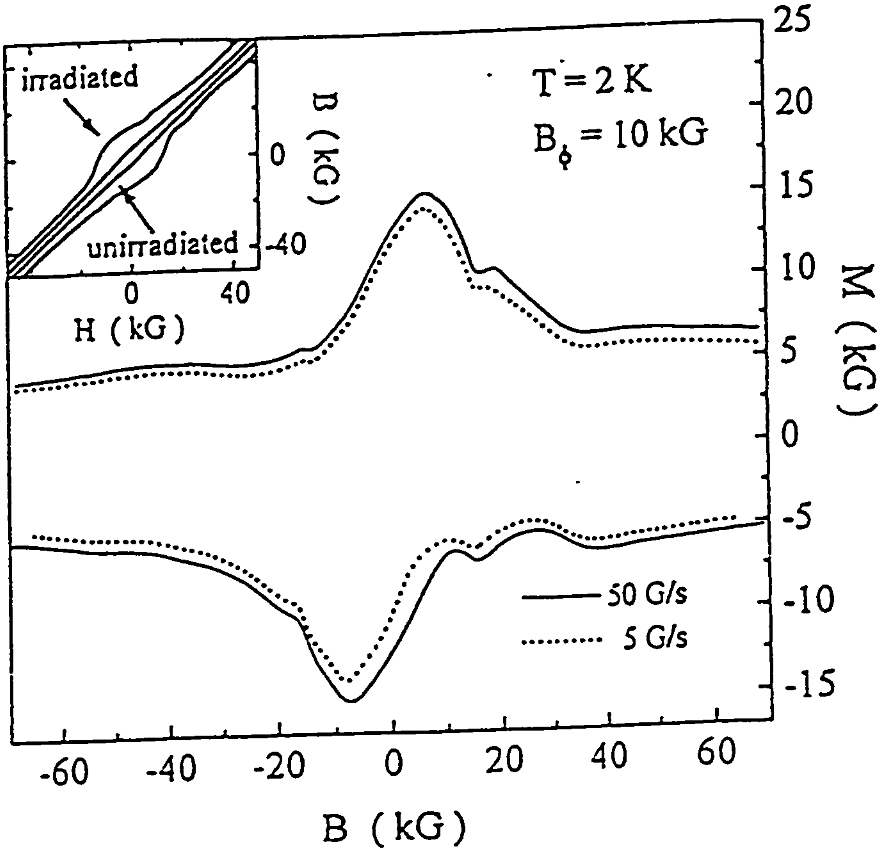

FIG. 1. Magnetization, M, vs local internal field, B, at $T=2$ K for the crystal with a columnar defect density corresponding to a vortex density at a field $B_\phi= 10$ kG. The hysteresis loop is narrower for slower sweep rates of the applied field. Data shown in subsequent figures correspond to the lower right-hand quadrant. Inset: columnar defects enlarge the hysteresis loop, particularly for $|B|<B_\phi$.

Fig. 2.5 Reproduced from Nowak et al[1]

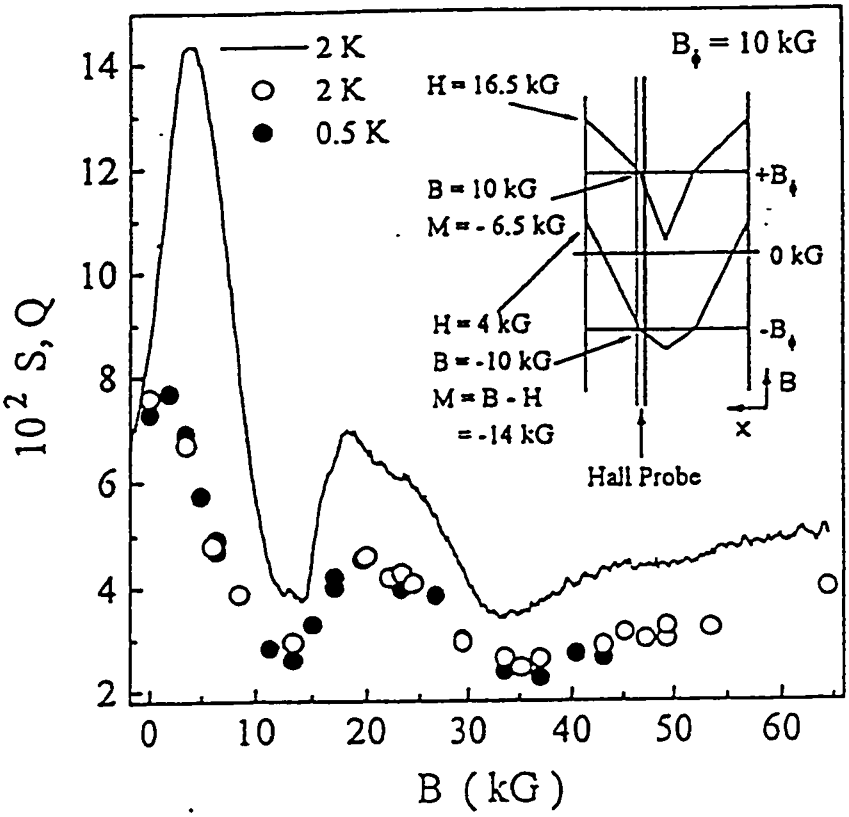

FIG. 3. Magnetization decay rates show sharp minima for internal fields near B_ϕ and $3B_\phi$. Symbols represent rate, S, determined with the applied field held constant. Solid line shows the dynamical rate, Q, calculated from the sweep rate dependence of the hysteresis loop. Inset: a model incorporating two critical currents in irradiated crystals can explain the maxima in the magnetization (Fig. 1) as the applied field is ramped up from large negative to large positive values.

Fig. 2.6 Reproduced from Nowak et al[1]

Fig 2.5 displays their measurements of the local magnetization $\mu_0 M(x) = B(x) - \mu_0 H_a$ versus $B(x)$. The inset displays $B(x)$ versus H_a. Five humps in $|M(x)|$ versus $B(x)$ can be discerned on careful inspection as $B(x)$ swings from a large positive value to a large negative value (upper curve) and similarly during the sweep in the opposite sense (lower curve). Note that, in principle, the curve in the 1st quadrant should be the "image" of that in the 3rd and the curve in the 2nd quadrant the image of that in the 4th. In chapter 3 we endeavour to reproduce these observations in the framework of the critical state model where we exploit a continuous but non-monotonic dependence of j_c on B.

Fig. 2.6 displays the observations of Nowak et al[6] for the local magnetic relaxation rate,

$$S(x) = dB(x)/\mu_0 M(x) d(\ln t) \qquad \textbf{(2.2)}$$

as a function of $B(x)$ at two different temperatures. They also display a related quantity denoted by the dynamical magnetization rate,

$$Q(B) = \ln\{M_f(B)/M_s(B)\}/\ln\{(dH_a/dt)_f/(dH_a/dt)_s\} \qquad \textbf{(2.3)}$$

versus $B(x)$. Here the subscripts f and s indicate that H_a was swept at a fast and a slow rate with corresponding data for the magnetization (see the solid and dashed curves of Fig. 2.5).

In Fig. 2.6 it is clear that regardless of the sweep rate and temperature they obtain curves with very similar structure with two distinct peaks and two minima. They emphasize that the bottom of the valleys are seen to correspond closely to B_ϕ and $3B_\phi$. In the figure caption they assert that "a model incorporating two critical currents can explain the maxima in the magnetization[16] (the previous figure). The insert in Fig 2.6 displays the model where $|\mu_O j_C| = |dB/dx|$ decreases abruptly as B traverses B_ϕ. This is the model that Beauchamp et al[8] exploited to reproduce their observations where only one peak (not five) was encountered (see Fig 2.3 and Fig. 1.3). Nowak et al[6] however do not demonstrate how this concept can generate their observations for the magnetic hysteresis (Fig. 2.5). They also do not present any quantitative model to account for the structure of their magnetic relaxation data. They do however put great emphasis on the feature that flux density at the minimum in the second valley corresponds to three times that for the first.

In the next two chapters we will present an empirical model which reproduces their observations displayed in Figs. 2.5 and 2.6. This model shows that the position of the summits of the $|M(x)|$ and of the valley minima in the $S(x)$ curves depends on, (i) the position of the probes and, (ii) whether $B(x)$ (hence H_a) is ascending or descending in magnitude. Consequently, the emphasis of Nowak et al[6] on the ratio of the positions of the minima being ≈ 3.0 is misleading. Our model indicates that the important ratio is that obtained for the two summits in the continuous but non-monotonic dependence of j_C on B. We find from our analysis of their data that this ratio $B_{S2}/B_{S1} \approx 2.5$. The difference between 2.5 and 3.0 is important for basic theoretical modelling of the interaction of the lattice of vortices with the lattice of columnar defects.

Chapter 3

Modeling of the Observed Local Hysteresis Curves

Introduction

In their paper Nowak et al[6] note that "it has recently been postulated (by Radzihovsky[10]) and shown (by Beauchamp et al[8]) that columnar defects lead to two critical current regimes as a function of internal field: an enhanced critical current in regions of the sample where $B < B_\phi$ for which each vortex is strongly pinned by a columnar defect, and a smaller critical current in regions where $B > B_\phi$ due to interstitial vortices that are less strongly pinned by point disorder and/or vortex interactions". Also in their paper Nowak et al state that, "a model incorporating two critical currents in irradiated crystals can explain the maxima in the magnetization (see Fig. 2.5) as the applied field is ramped up from large negative to large positive values".

In this chapter I first demonstrate that the "staircase" type of dependence of j_c on B mentioned above, (i) can only account for the maximum in $|M(x)|$ versus $B(x)$ occurring adjacent to $B(x) = 0$, and (ii) cannot account for the valleys and adjacent summits in $|M(x)|$ observed at higher values of $B(x)$ (see Fig. 2.5). In particular, I show that valleys in $|M(x)|$ versus $B(x)$ require the existence of corresponding valleys in j_c versus B. Then I present our application of the critical state concept to account for the observations of Nowak et al[6] of peaks and valleys in the curves of the local magnetization $\mu_0 M(x) = B(x) - \mu_0 H_a$ versus $B(x)$ of a single crystal of $Tl_2Ba_2CuO_{6+\delta}$ with columnar defects (see Fig. 2.5).

The Radzihovsky/Beauchamp et al Model

Beauchamp et al[8] applied a model for the dependence of j_C on B proposed by Radzihovsky[10] to analyse their observations of the evolution of $B(x)$, the local magnetic flux density in their irradiated YBCO single crystals as the externally applied magnetic field H_a was made to vary from a large negative value through zero to a large positive value and vice versa.

Radzihovsky[10] argued that the critical current density $j_c(B)$ should be considerably enhanced when $B(x)$ lies below the matching field B_ϕ since here each of the flux lines can be regarded as condensing on or occupying a columnar defect. Hence this situation is described as the Strong Bose Glass phase of the vortex lattice. Since the columnar defects are randomly distributed, this condensed phase is, by analogy, denoted glassy or amorphous. When $B(x)$ is larger than B_ϕ, all of the columnar defects are occupied and the migration of the excess interstitial vortices is now impeded only by their interaction with the flux lines pinned by the defects. Indeed this interaction (mutual repulsion) can lead to a depinning of the "condensed" vortices. As a consequence, the displacement of the lattice of flux lines is now only weakly opposed by the columnar defects. Therefore the critical current density $j_c(B)$ is seen to diminish abruptly when $B(x)$ traverses the B_ϕ boundary. The rapid decrease of $j_c(B)$ at B_ϕ is, again by analogy, denoted as a Mott Insulator transition and the regime of $B(x)$ above B_ϕ as the Weak Bose Glass phase.

Beauchamp et al[8] therefore postulated a single step staircase type of dependence of j_C on B as shown schematically in Fig. 3.1. In their analysis these workers introduced only one break at B_ϕ in the structure of $j_c(B)$ since they sought to account for the single peak they observed in their measurements of $M(x)$ versus $B(x)$. However since Nowak et al[6] observe several peaks we have extended the Radzihovsky[10] picture in Fig. 3.1 and introduced a second step in j_C versus B with a "discontinuity" arbitrarily located at 3 B_ϕ for the purpose of illustration.

Clearly the crude dependence of j_C on B displayed in Fig. 3.1 can be refined while remaining faithful to the basic concepts developed by Radzihovsky[10] in this context. In such refinements the flat segments would exhibit some dependence of j_C on B and the vertical segments would acquire a finite slope.

We now show that any staircase type of dependence of j_C on B can only lead to a staircase type of variation of $M(x)$ versus $B(x)$. This can be seen quite generally and readily by noting that,

$$\mu_o M(x_p) = B(x_p) - \mu_o H_a = \int_{\mu_o H_a}^{B(x_p)} dB = \pm\mu_o \int_0^{x_p} j_c(B(x))dx = \pm\mu_o < j_c(B(x)) > x_p \qquad \textbf{(3.1)}$$

where $< j_c(B(x)) >$ is the spatial average of $j_c(B(x))$ between the surface x = 0 and x = x$_p$, the location of the probe measuring $B(x)$. From inspection of eqn. 3.1 we can see that $|M(x_p)|$ must decrease monotonically as a function of $|< j_c(B(x)) >|$. Consequently $|< j_c(B(x)) >|$, hence $j_c(B(x))$, must exhibit

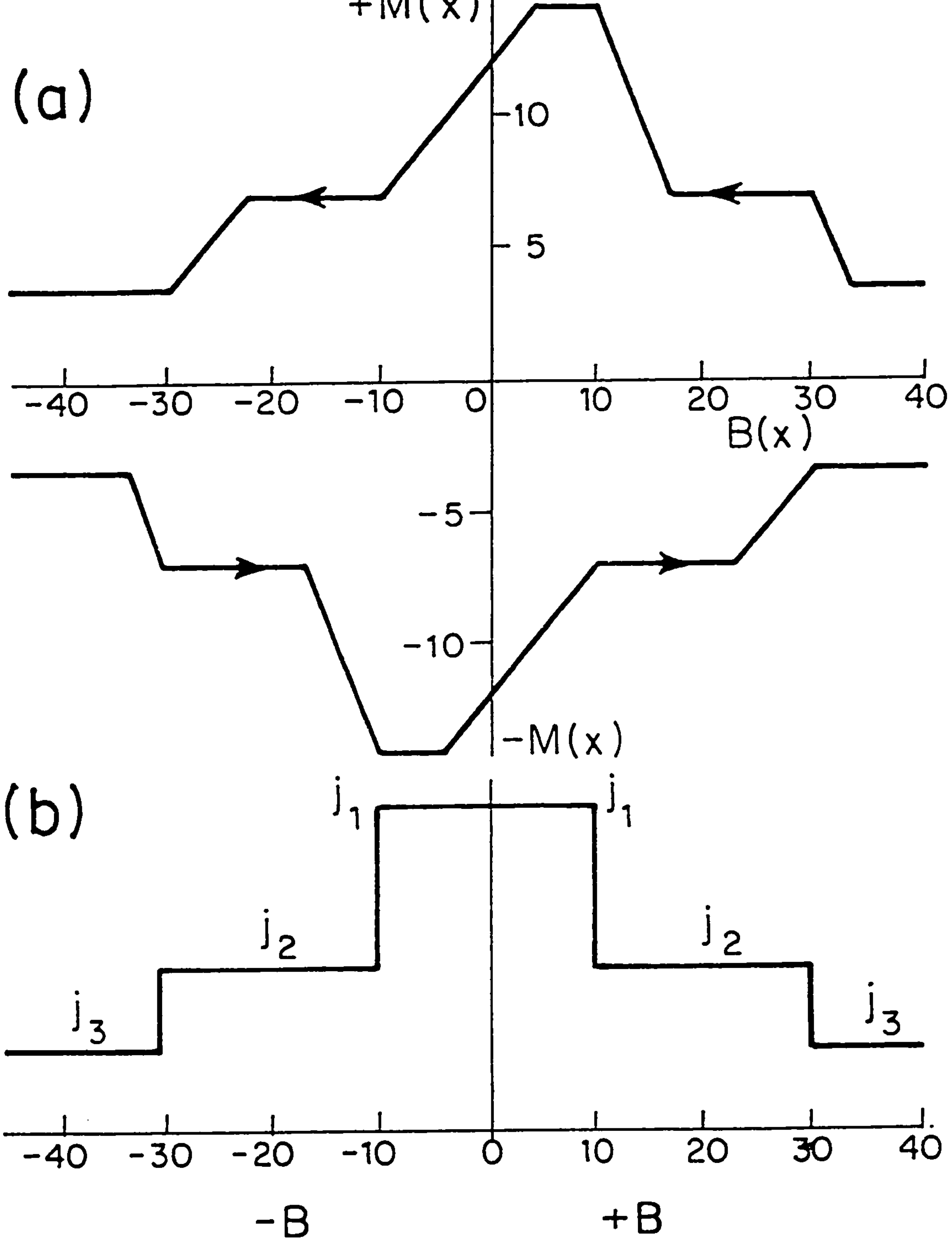

Fig. 3.1 The staircase type of dependence of j_c on B as postulated by Radzihovsky is shown in (b) with the resulting $|M(x)|$ versus $B(x)$ given in (a). Here it is clear that the step-like function cannot generate the minima in $|M(x)|$.

maxima and minima in order that $|M(x_p)|$ versus $B(x)$ trace maxima and minima.

Finally we note that the summits traced by $|M(x)|$ adjacent to $B(x) = 0$ in Fig. 3.1(a) arise from the feature that $j_c(B)$ also displays a peak between $+B_\phi$ and $-B_\phi$ in Fig. 3.1(b). The detailed structure depicted in Fig. 3.1(a) was calculated by introducing numerical values for j_1 and j_2 extracted from the observations of Nowak et al[6] (see the inset of Fig. 2.6).

Framework and Results of the Model

The dependence of j_C on B which we exploit is displayed in Fig. 3.2. For simplicity we choose the well known Kim[11] type of expression for the "background" curve of j_C versus B,

$$j_C = j_O\left(\frac{B_{ref}}{B + B_O}\right)^n \qquad \textbf{(3.2)}$$

where we assume that the temperature dependent parameters, j_O, B_{ref}, B_O and n will vary with the heavy ion irradiation.[6-9,12-20] The two peaks in j_C versus B which are superimposed on this background are, for simplicity, chosen to be "triangular" with symmetric slopes on the left and right of the maxima. Therefore we write,

$$j_{C1L}(B(x)) = j_{S1}\left(\frac{B(x) - B_{A1}}{B_{S1} - B_{A1}}\right), \qquad j_{C1R} = j_{S1}\left(\frac{B_{B1} - B(x)}{B_{B1} - B_{S1}}\right) \qquad \textbf{(3.3)}$$

for the left and right sides of the first peak and similarly,

$$j_{C2L}(B(x)) = j_{S2}\left(\frac{B(x) - B_{A2}}{B_{S2} - B_{A2}}\right), \qquad j_{C2R} = j_{S2}\left(\frac{B_{B2} - B(x)}{B_{B2} - B_{S2}}\right) \quad \textbf{(3.4)}$$

for the second peak. Equations 3.3 and 3.4 apply between their respective boundaries, $B_{\phi 1L}$, $B_{\phi 1R}$, $B_{\phi 2L}$ and $B_{\phi 2R}$. The magnitudes of the critical current densities, j_{S1} and j_{S2} at the summit of the two peaks as well as the width of the bases of the peaks and their location are presumably determined by the irradiation which also affects the structure and magnitude of the background curve.[6-9,12-20] In the modeling, the choices for these six quantities dictate the values for B_{A1}, B_{B1}, B_{A2} and B_{B2}.

The various parameters which quantitatively specify j_C versus B displayed in Fig. 3.2 are selected to yield a good fit to the data reported by Nowak et al[6] for $M(x)$ versus $B(x)$ ascending in magnitude (see Fig. 2.5) and are listed in the caption to figure 3.2.

The sequences of critical state profiles of $B(x)$ versus H_a ascending or descending in magnitude are developed from Maxwell's equation, $\nabla \times \bar{B} = \mu_0 \bar{j}$, hence, $dB/dx = \pm\mu_0 j_C(B(x))$ for an idealized slab geometry or, $dB/dr = \pm\mu_0 j_C(B(r))$ for an infinite cylinder. We ignore intrinsic diamagnetism, hence take $B(x) = \mu_0 H(x)$ and the magnetic flux density just inside the surface of the specimen, $B_i = \mu_0 H_a$ where H_a is the applied magnetic field.

It is a straightforward albeit tedious exercise to develop detailed expressions for the large variety of critical $B(x)$ profiles which are encountered as the upward and downward sweeps of H_a generate configurations which successively incorporate the detailed structure of jc versus B displayed in Fig. 3.2. Some illustrative examples of the sequences of $B(x)$ profiles are displayed in Figs. 3.3 and 3.4 and in the appendix. Typical expressions for $B(x)$ versus H_a are developed in the appendix.

Fig. 3.5 displays the results of our calculation of $M(x)$ versus $B(x)$ in a two quadrant format and should be compared with the right half of Fig. 2.5. The peak labeled $P\downarrow$ in Fig. 3.5 is generated by the "background" $j_C(B)$ function (i.e. eqn. 3.2) which, although affected by the heavy ion irradiation, is not directly linked to the matching field B_ϕ. This peak is also present in the measurements of Beauchamp et al[7,8] (see Figs. 2.1, 2.2 and 2.3(a)). The choice of n, B_{ref} and B_O determine the structure and location of this peak and its magnitude is fixed by the choice of j_O. We note that, in agreement with the observations, the two peaks $P_1\uparrow$ and $P_2\uparrow$ with $|M(x)|$ versus H_a ascending are displaced with respect to the corresponding peaks $P_1\downarrow$ and $P_2\downarrow$ where H_a is descending in magnitude. Thus, the selection for the location of the triangular peaks in j_C versus B in our model (Fig. 3.2) correctly determines the location of the peaks in $|M(x)|$ versus $B(x)$ descending and ascending in magnitude.

Close examination of Fig. 3.4 also shows that the four peaks ($P_1\uparrow, P_2\uparrow, P_1\downarrow$ and $P_2\downarrow$) display asymmetries in agreement with that exhibited by the measured peaks. The asymmetry in the theoretical peaks of

$|M(x)|$ versus $B(x)$ arises from the following features in the variation of j_C versus B. The "background" j_C (eqn. 3.2) is larger on the left of a triangular peak than on its right (see Fig. 3.2), and, as a consequence the left side of a triangular peak is narrower than its right side although the magnitude of the two slopes are identical. The asymmetry in the humps of $|M(x)|$ versus $B(x)$ is therefore generic in our model and will also appear if exponential, gaussian or other centrosymmetric humps for j_C versus B were introduced instead of centrosymmetric triangular peaks.

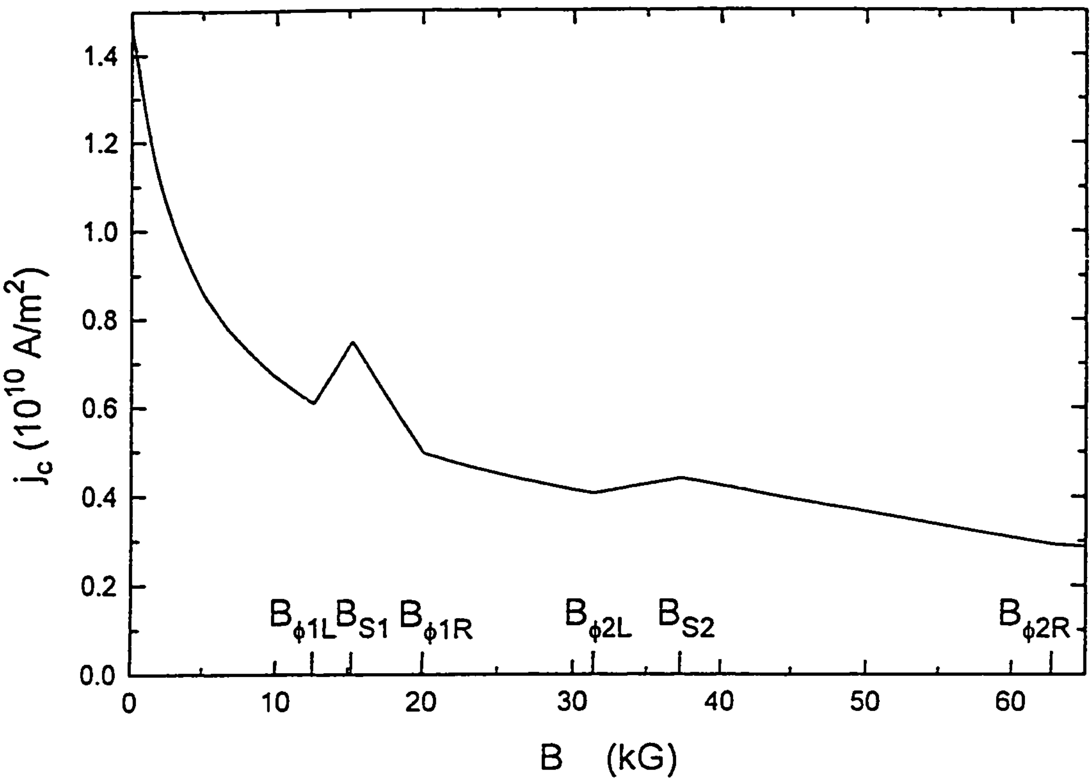

Fig. 3.2. Display of j_c versus B (eqns. 3.2, 3.3, 3.4) used in our modeling of the pertinent observations (Figs. 2.5 and 2.6 in this thesis reproducing Figs. 1 and 3 of Nowak et al[6]). For the "background" curve (eqn. 3.2) we chose $n = 1/2$, $B_O = 2.5$ kG, $B_n = \left(3\mu_O j_O X B_{ref}^{1/2}/2\right)^{2/3} = 12.5$ kG and for the triangular peaks we let $B_{\phi 1L}$, B_{S1}, $B_{\phi 1R}$, $B_{\phi 2L}$, B_{S2} and $B_{\phi 2R}$ equal to 12.5, 15.2, 20, 31.25, 37.14 and 62.5 kG while $j_{S1} = 1.125$ (10^{10}) kG and $j_{S2} = 0.66$ (10^{10}) kG. The parameters were selected to yield a good fit to the curve of $|M(x)|$ versus $B(x)$ ascending in magnitude reported by Nowak et al[1]. The model addresses idealized slab or cylinder geometry with $X = R = 100$ µm. Triangular peaks were selected for analytic and computational convenience. We note that $B_{S2}/B_{S1} \approx 2.5$.

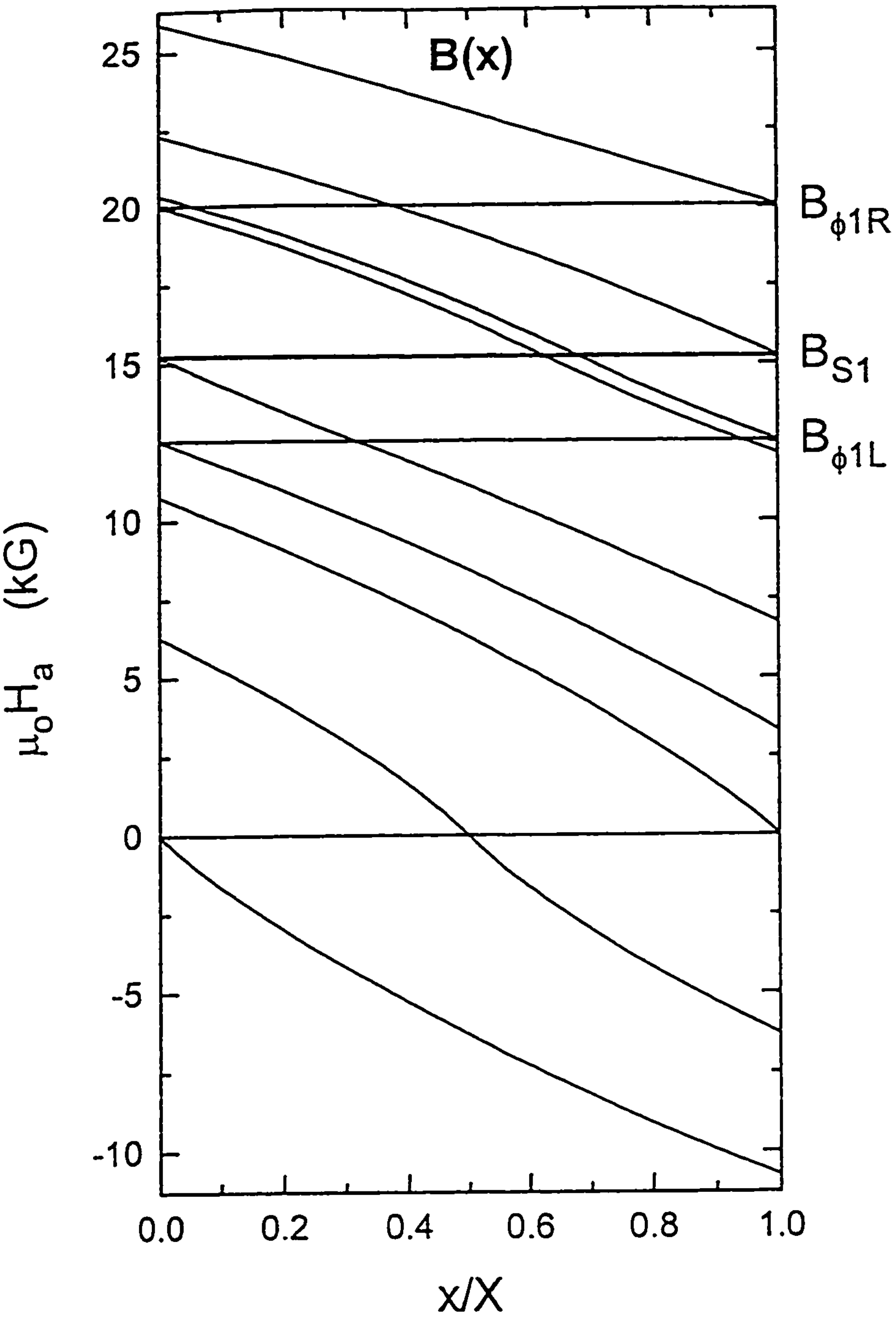

Fig. 3.3. Displays an illustrative sequence of $B(x)$ profiles generated by $j_C(B)$ of Fig. 3.2. Here after descending in magnitude from the "negative" direction $\mu_0 H_a$ is now ascending in the opposite direction from zero through $B_{\phi 1L}$, B_{S1} and $B_{\phi 1R}$, hence across the first peak of $j_C(B)$. The surface of the specimen is situated at $x/X = 0$ and its center at $x/X = 1$.

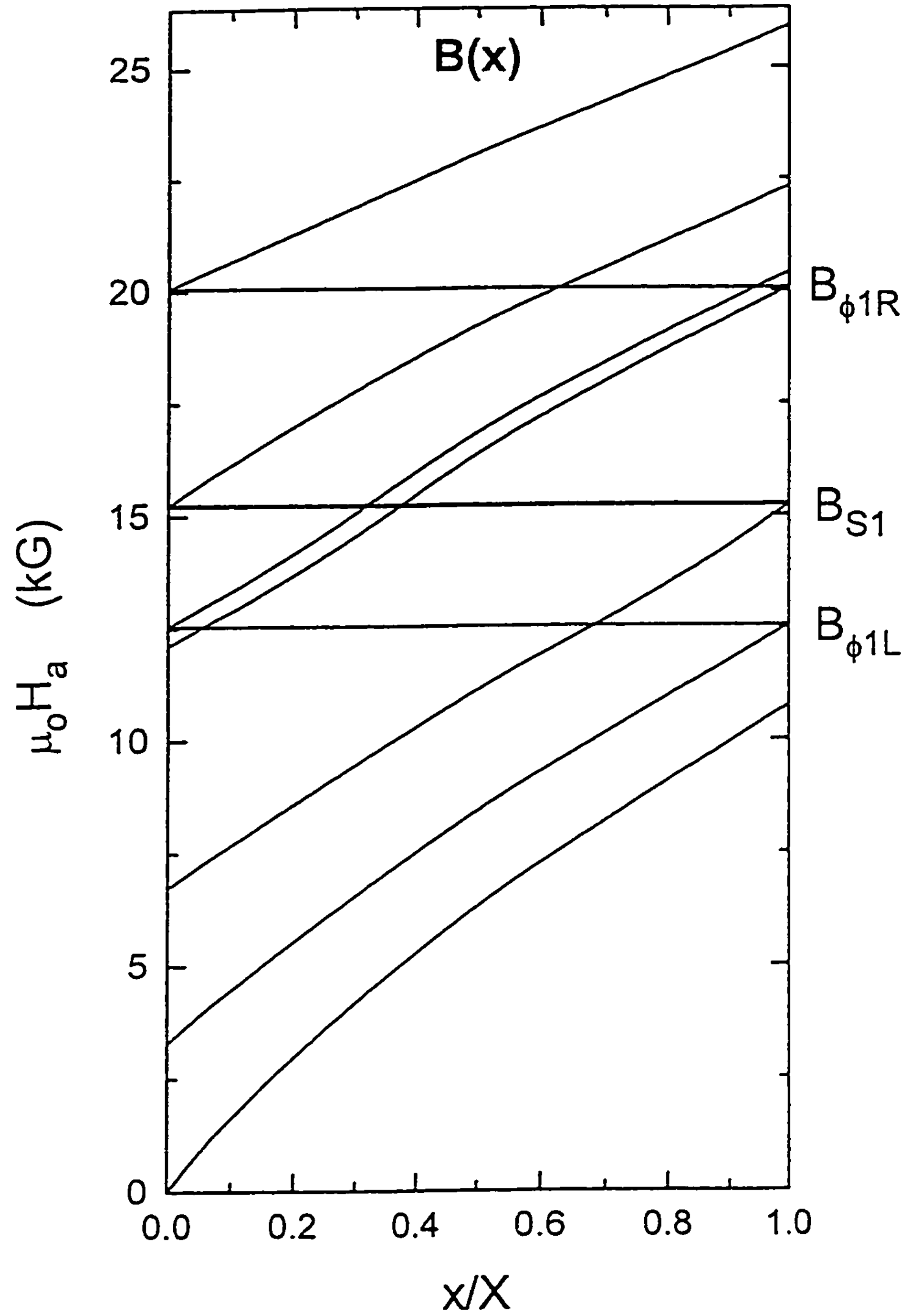

Fig. 3.4. Complements the previous figure by displaying a sequence of $B(x)$ profiles where now $\mu_0 H_a$ is descending in magnitude from a large value.

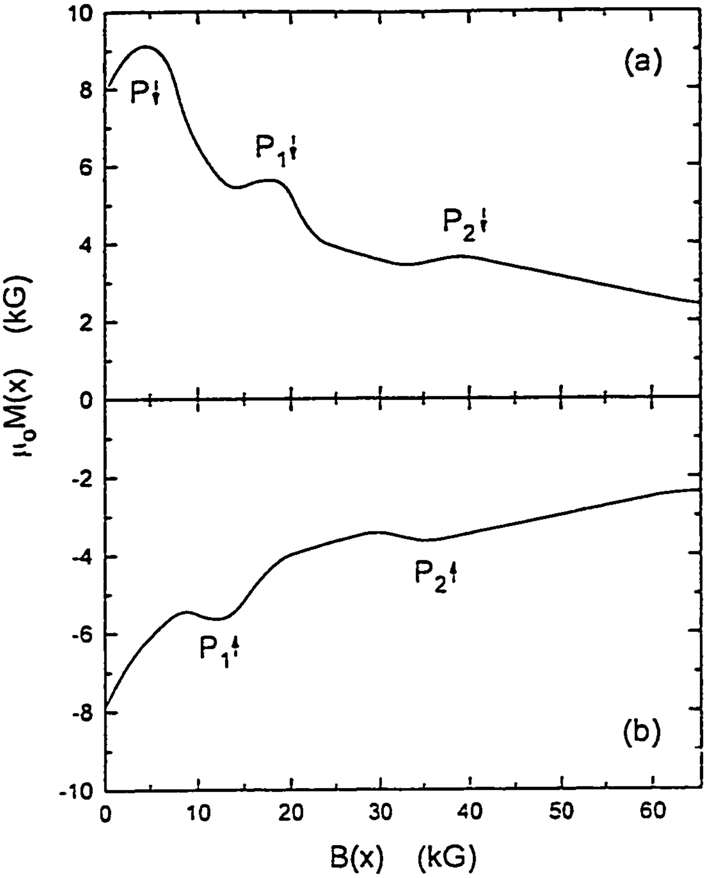

Fig. 3.5. Displays the local magnetization, $\mu_0 M(x) = B(x) - \mu_0 H_a$ versus $B(x)$ which is generated by $j_C(B)$ of Fig. 3.2 when $B(x)$ is descending (a) and ascending (b) in magnitude. These two calculated curves should be compared with that presented in the right half of Fig. 2.5. The height, breadth and position of the salient features of these curves are modified when the location x/X of the measuring probe is changed. In particular, the position of the summits of the peaks $P_1 \downarrow$ and $P_1 \uparrow$ approach B_{S1} while $P_2 \downarrow$ and $P_2 \uparrow$ approach B_{S2} as the location of the measuring probe, x/X, is moved closer to the surface of the specimen. However this also causes $|M(x)|$ to diminish. The reason for this emerges from careful examination of representative $B(x)$ profiles shown in Figs. 3.3 and 3.4. We took $x/X = 2/3$ in the calculations for $M(x)$ and $B(x)$ since this corresponds to the position of the field probe in the measurements reported by Nowak et al[6]. "Ideally" in Fig. 2.5 (Nowak et al[6]), the curve in the first (fourth) quadrant should be the exact "image" of that in the third (second) quadrant.

Chapter 4

Modeling of the Local Flux Creep Rates

Introduction

In this chapter I present an application of the critical state concept to account for the observations of Nowak et al[6] of peaks and valleys in the curves of the local flux density creep rate $S(x)$ versus $B(x)$ of a single crystal of $Tl_2Ba_2Cu_3O_{6+\delta}$ with columnar defects (see Fig. 2.6). To reproduce their data we introduce two simple assumptions. The agreement we obtain with their observations indicate that these two simple assumptions are valid approximations.

Framework and Results of the Model

The rate of local relaxation of the flux density profiles can be written,

$$S(x) = \frac{dB(x)}{dt} = \frac{dB(x)}{dj_O}\frac{dj_O}{dt} = R(x)\frac{dj_O}{dt} \qquad \textbf{(4.1)}$$

where it is assumed that dj_O/dt does not depend on $B(x)$. We focus on the relative rate, $R(x) = dB(x)/(dj_O/j_O)$ and on the normalized rate, $R_n(x) = dB(x)/(\mu_O M(x) dj_O/j_O)$.

Our treatment is a simple extension of an approach already exploited by several workers.[10,21-24] In this framework the decay of the critical state configuration is determined by the decrease of the current density parameters j_O, j_{S1} and j_{S2} in eqns. 3.2, 3.3 and 3.4. As the parameter j_O of the background curve (eqn 3.2) decreases by an amount Δj_O we visualize that $j_C(B)$ along the triangular summits decays as illustrated schematically in Fig. 4.1. The diminution of j_C at the summits can be written,

$$\frac{\Delta j_{S1}}{j_{S1}} = f_1 \frac{\Delta j_O}{j_O} \quad \text{and} \quad \frac{\Delta j_{S2}}{j_{S2}} = f_2 \frac{\Delta j_O}{j_O}. \qquad \textbf{(4.2)}$$

We obtain good agreement with the pertinent data of Nowak et al[6] (see Fig. 2.6) by letting $f_1 = f_2 = 1/2$. We assume, for simplicity, that the rate of decay of $j_C(B)$ along the slopes of the triangular summits varies linearly versus $B(x)$ from its value at the junctions with the background curve (i.e. the boundaries $B_{\phi 1L}$, $B_{\phi 1R}$, $B_{\phi 2L}$ and $B_{\phi 2R}$) to a smaller value at the summits, B_{S1} and B_{S2}. (i) The continuity of $j_C(B)$ at the boundaries and, (ii) the constraint that the location of these boundaries as well as the location of the summits along the B axis remain fixed, as j_O, j_{S1} and j_{S2} diminish, dictate the evolution B_{A1}, B_{B1}, B_{A2} and B_{B2} in eqns. 3.3 and 3.4, hence determine the relaxation of the flux density profiles. The results of this exercise are displayed in Figs. 4.2 through 4.5 where for completeness and clarity we present both R_n and R, the normalized and unnormalized relative relaxation rates for $B(x)$ increasing and decreasing in magnitude. We note, however, that the normalized relaxation rate, a composite quantity of two components, has the drawback that it contains the experimental errors or modeling approximations of the two constituents.

Fig. 4.2 is seen to reproduce the major features of the pertinent observations of Nowak et al[6] (see Fig. 2.6). The fact that $B_{V1}\uparrow$ and $B_{V2}\uparrow$, the location of the bottom of the two valleys, corresponds to that encountered by Nowak et al[6], hence closely match B_ϕ and $3B_\phi$, ensues from our choices for the parameters, $B_{\phi 1L}$, $B_{\phi 1R}$, j_{S1}, $B_{\phi 2L}$, $B_{\phi 2R}$ and j_{S2}, which were selected to account for the location, magnitude and structure of the peaks ($P_1\uparrow, P_2\uparrow, P_1\downarrow$ and $P_2\downarrow$) in the local hysteresis curves (see Fig. 3.5). The depths of the valleys relative to their shoulders is mainly controlled by the choices for f_1 and f_2. Asymmetry in the structure of the valleys arises from the same feature that causes the asymmetry of the peaks in Fig. 3.5, namely that $(B_{\phi 1R} - B_{S1}) > (B_{S1} - B_{\phi 1L})$ and $(B_{\phi 2R} - B_{S2}) > (B_{S2} - B_{\phi 2L})$ for the centrosymmetric triangular peaks (see Figs. 3.2 and 4.1).

In our model, the peak straddling $B(x) = 0$ arises from the large j_C at low fields and its strong dependence on magnetic flux density.[9] The latter properties are produced by the heavy ion irradiation.[7,12-20] The feature that the measured peak is not centered at $B(x) = 0$ may be due to the large demagnetization factor encountered with the platelet specimens in the experiments.

The model generates detailed predictions regarding the evolution of, (i) the position along the $B(x)$ axis of the bottom of the valleys, and, (ii) the structure of these valleys as a function of the location x/X of the measuring probes. We note that $B_{V1}\uparrow$ and $B_{V2}\uparrow$, the location of the bottom of the valleys along the $B(x)$ axis occurs at slightly lower fields than B_{S1} and B_{S2}, the summits of the triangular peaks in j_C versus B (see Fig. 3.2). In our model, the values of the former depends on the location of the measuring probe (see the appendix). Here $B_{V2}\uparrow/B_{V1}\uparrow\approx 2.8$ whereas $B_{S2}/B_{S1}\approx 2.5$.

The "acid test" of the predictive value of the model however resides mainly in the curves it generates for R and R_n (hence $S(x)$ and $S_n(x)$) versus $B(x)$ descending in magnitude. These predictions are displayed in Figs. 4.4 and 4.5. The first low field valley appearing in the graph of $R_n(x)$ versus $B(x)$ descending in magnitude is, in a sense, an artifact of the normalization with respect to $|M(x)|$ since the latter traces a pronounced peak in this range of $B(x)$ (see the upper curve of Fig. 3.5). Note that $B_{V1}\downarrow$ and $B_{V2}\downarrow$, the bottoms of the valleys when $B(x)$ is descending in magnitude appear at significantly higher fields than B_{S1} and B_{S2}, the summits of the triangular peaks in $j_C(B)$. An important related consequence is that the ratio $B_{V2}\downarrow/B_{V1}\downarrow\approx 2$ is appreciably smaller than the ratio $B_{S2}/B_{S1}\approx 2.5$ and hence smaller than the ratio $B_{V2}\uparrow/B_{V1}\uparrow\approx 3$. Again, we stress that in our model, $B_{V1}\downarrow$, $B_{V2}\downarrow$, and their ratio depend on the location of the measuring probe.

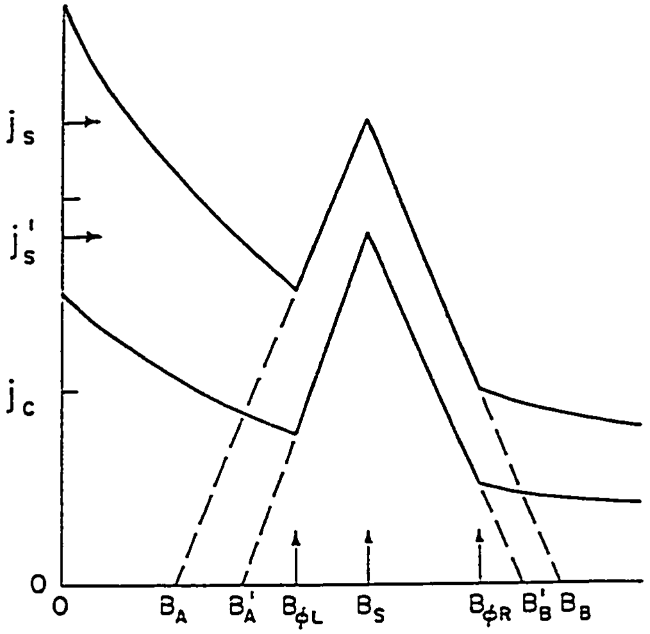

Fig. 4.1. Schematically illustrates the decay of the critical current density introduced in our model. We visualize that, during the decay, the location on the B axis of the boundaries ($B_{\phi 1L}, B_{\phi 1R}$, $B_{\phi 2L}$ and $B_{\phi 2R}$) and of the summits (B_{S1} and B_{S2}) of the triangular peaks (only one shown) remains fixed. The rate of decay of the critical current density $j_C(B)$ is assumed independent of the flux density for the background curve (eqn. 3.2) but to vary smoothly at the boundaries and linearly along the slopes of the triangular peaks. Good agreement with the data displayed in Fig. 2.6 (Nowak et al[6]) is obtained letting the rate of decay, $\Delta j_{S1}/j_{S1}$ and $\Delta j_{S2}/j_{S2}$, at the summits of the triangular peaks to be $\approx 1/2\,\Delta j_O/j_O$, hence 1/2 the decay rate at the boundaries of the peaks, and to vary linearly along the slopes of the triangular peaks. Initially, for simplicity, we take the triangular peaks to be centrosymmetric hence let $B_{S1} = (B_{A1} + B_{B1})/2$ and $B_{S2} = (B_{A2} + B_{B2})/2$. As j_C decays with the location of the boundaries and summit of the triangular peaks remaining fixed, the bases of the triangles, B_{A1}, B_{B1}, B_{A2} and B_{B2} (see eqns. 3.2 and 3.3) migrate to new values, denoted B'_{A1}, B'_{B1}, B'_{A2} and B'_{B2}. Also, the left slope of a triangular peak becomes steeper than that on its right, hence now $B_{S1} \neq (B'_{A1} + B'_{B1})/2$ and $B_{S2} \neq (B'_{A2} + B'_{B2})/2$. The continuity of $j_C(B)$ at the boundaries (eqns. 3.2,3.3 and 3.4) yield 0.933, 29.54, -33.188 and 113.08 kG for B_{A1}, B_{B1}, B_{A2} and B_{B2}. For clarity, the amount of decay of $j_C(B)$ is greatly exaggerated in the figure.

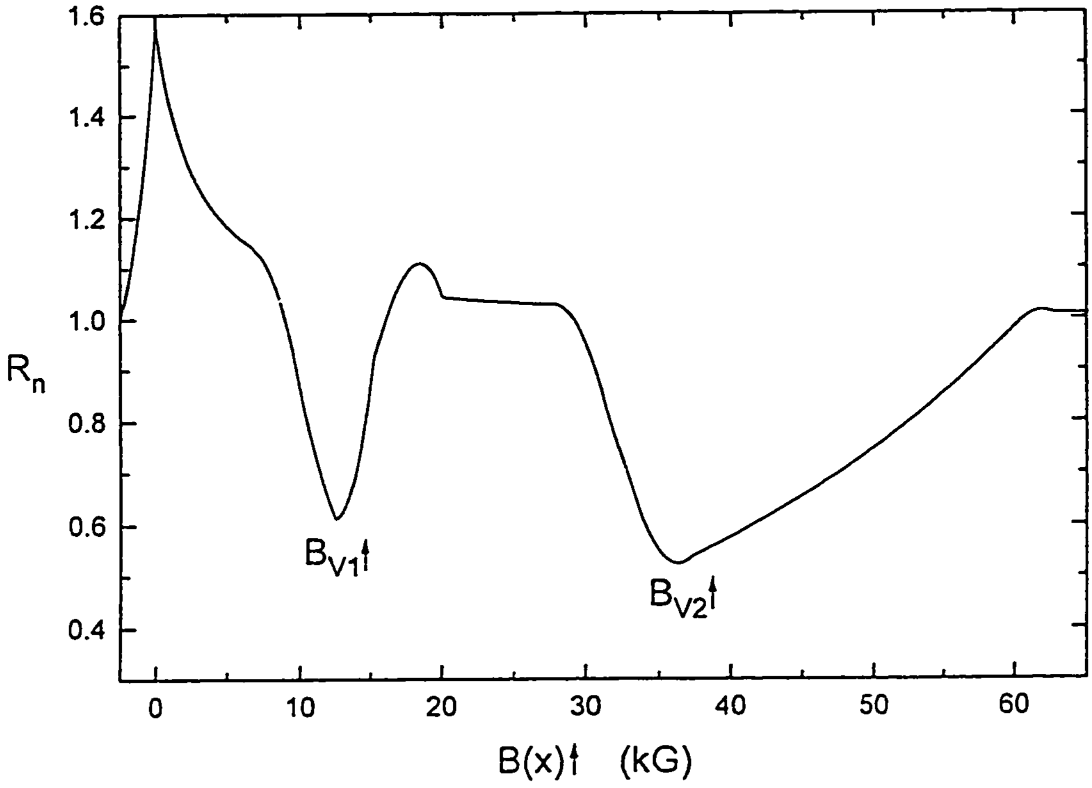

Fig. 4.2 Displays the normalized initial relaxation rate, $R_n = |\Delta B(x)/\mu_0 M(x)(\Delta j_0/j_0)|$ versus $B(x)$ calculated for $x/X = 2/3$ using the decay of $j_C(B)$ schematically illustrated in Fig. 4.1. Here $B(x)$ after descending in magnitude through zero is ascending in magnitude in the opposite direction (see our Fig. 2.5, Nowak et al[6]). This "theoretical" curve should be compared with the curve traced by the open circle data of our Fig. 2.6 (Nowak et al[6]). The salient features of the structure of the theoretical curve persist but absolute and relative values of $M(x)$ change with the location of the measuring probe. In particular, the position of the minima, $B_{V1}\uparrow$ and $B_{V2}\uparrow$ approach B_{S1} and B_{S2}, hence the ratio, $B_{V2}\uparrow/B_{V1}\uparrow$ approaches $B_{S2}/B_{S1} \approx 2.5$ from above as the probe is placed closer to the surface of the specimen. Careful consideration of Figs. 3.3 and 4.1 indicate why this occurs with our model.

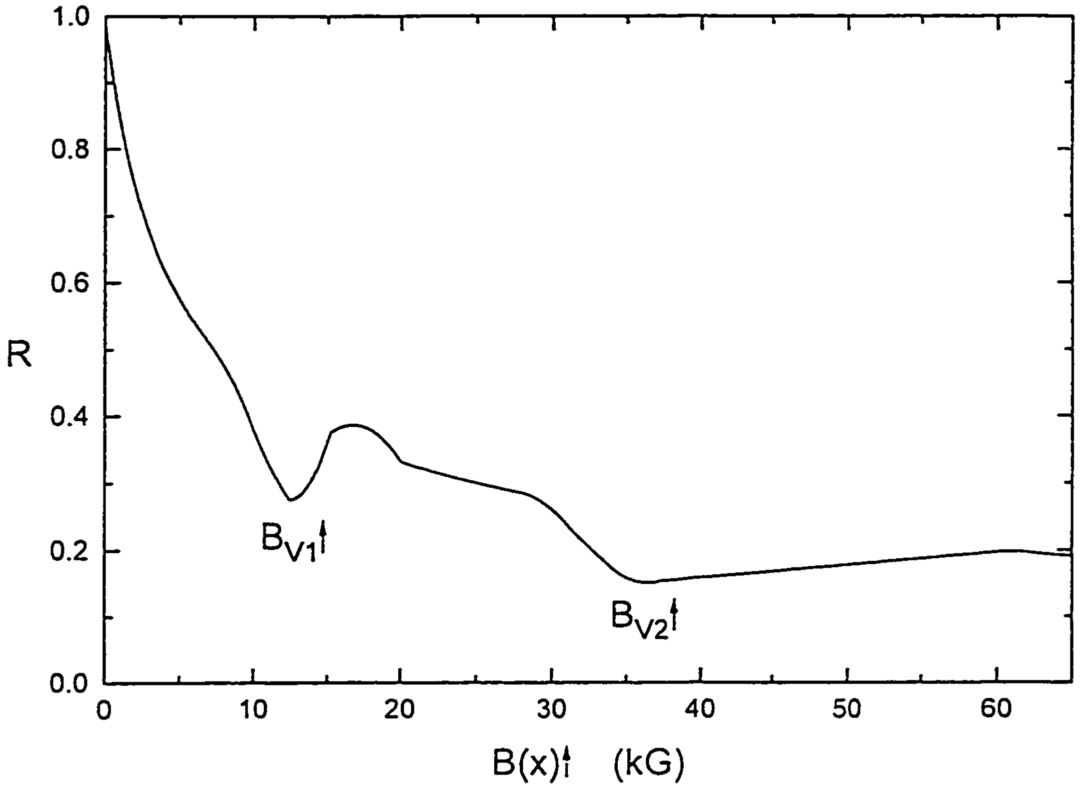

Fig. 4.3 Complements (a) by displaying the corresponding initial relaxation rate, $R = \left|\Delta B(x)/B_n\left(\Delta j_O/j_O\right)\right|$ versus $B(x)$, hence here the separately calculated (and measured) quantity $M(x)$ is not introduced. For convenience however $B(x)$ is normalized with respect to the parameter $B_n = \left(3\mu_O j_O X B_{ref}^{1/2}/2\right)^{2/3}$. When $B(x) = 0$, $R = (2/3)(x/X)/(B_O/B_n)^{1/2}$ (see appendix) hence the feature that here $R(0) \approx 1.0$ is coincidental and a consequence of our choices for x/X and B_O/B_n.

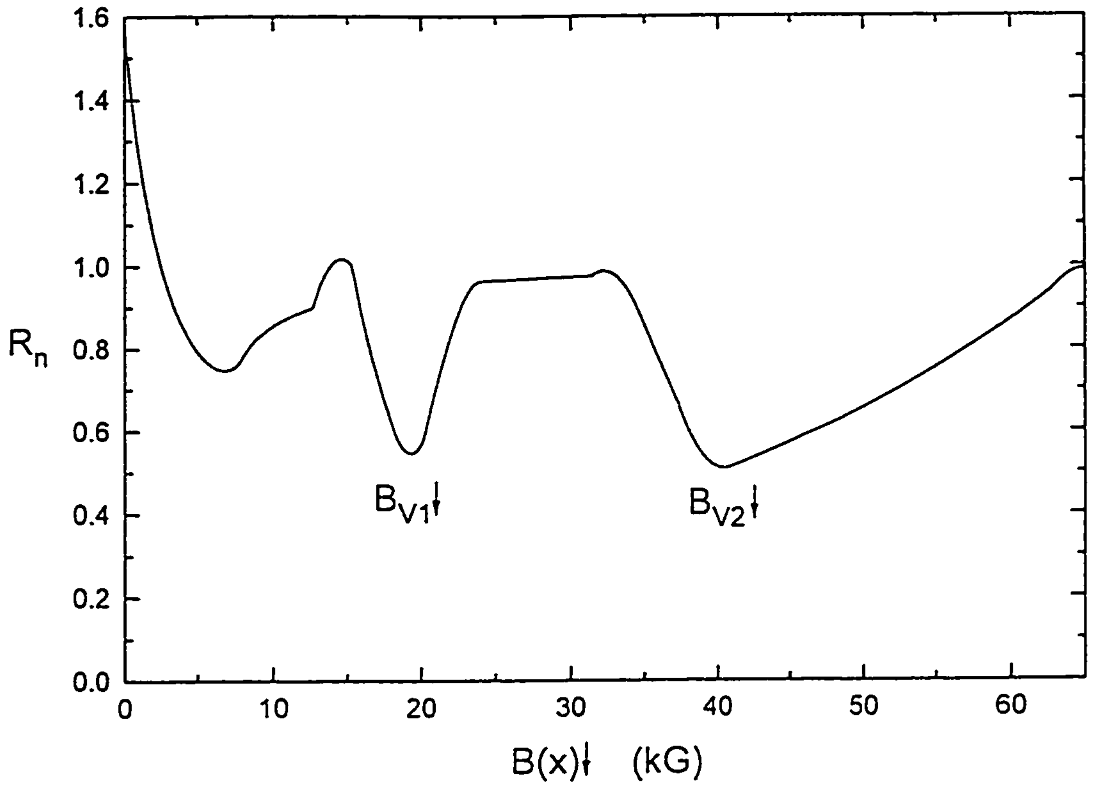

Fig. 4.4. Complements Fig. 4.2 by displaying the corresponding "predicted" initial relaxation rate R_n where now $B(x)$ is descending in magnitude from a large value. Nowak et al[6] do not report on the relaxation rate under these circumstances. Comparing these curves with the corresponding curves of Fig. 4.2 we note that the model predicts that, for any chosen location of the measuring probe, $B_{V1}\downarrow > B_{V1}\uparrow$, $B_{V2}\downarrow > B_{V2}\uparrow$, and $B_{V2}\downarrow/B_{V1}\downarrow < B_{V2}\uparrow/B_{V1}\uparrow$. Further $B_{V1}\downarrow$ and $B_{V2}\downarrow$ approach B_{S1} and B_{S2} hence the ratio, $B_{V2}\uparrow/B_{V1}\uparrow$ approaches $B_{S2}/B_{S1} \approx 2.5$ from below as the probe is placed closer to the surface of the specimen. Again, careful consideration of Figs. 3.4 and 4.1 indicates that these results are generic features of our model hence do not depend on our choice of a triangular structure for the peaks in $j_C(B)$ and our simple prescription for the "background" decrease of j_C versus B.

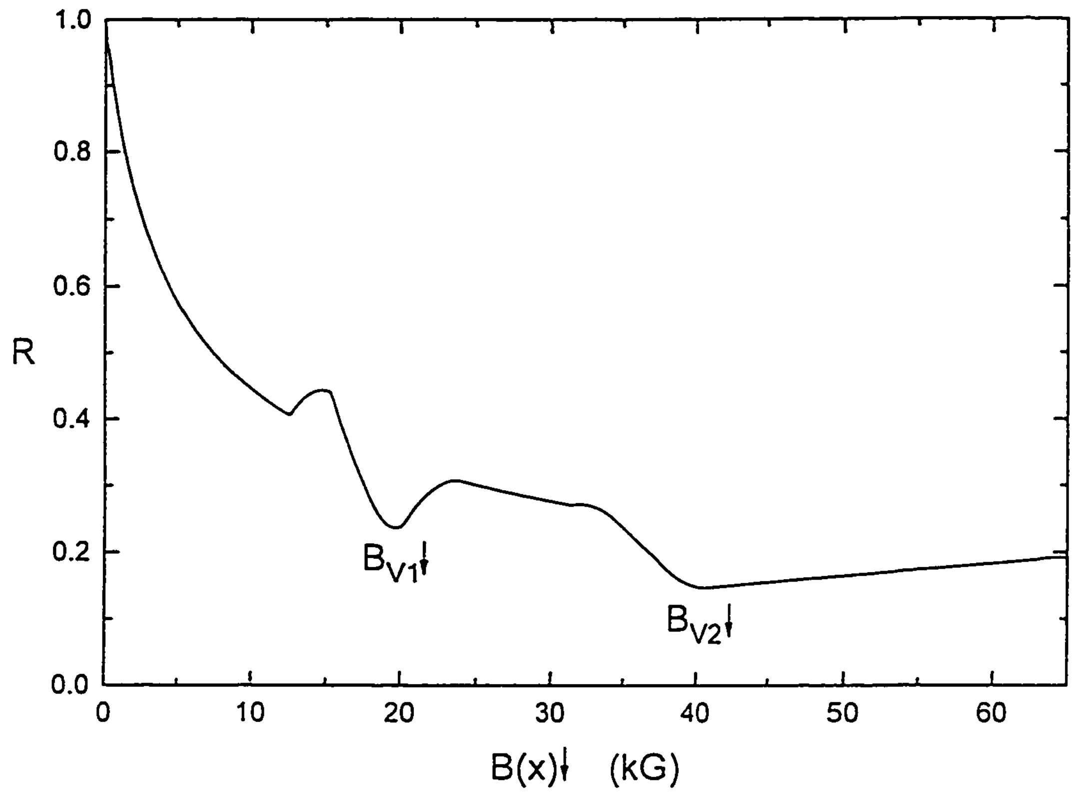

Fig. 4.5 Complements Fig. 4.3 by displaying the corresponding "predicted" initial relaxation R where now $B(x)$ is descending in magnitude from a large value.

Chapter 5

Summary and Conclusion

We have developed an empirical model which semi-quantitatively accounts for the location and structure of peaks in the local magnetization $|M(x)|$ and a central peak and valleys in the local relaxation rate $R_n(x)$ versus $B(x)$ observed by Nowak et al[6] in a single crystal of an anisotropic high T_C superconductor containing columnar defects. In agreement with observations, the location of the peaks and valleys and their structure depend on (i) whether $B(x)$ is ascending or descending in magnitude and, (ii) the position of the measuring probes. As a consequence the ratios for the values observed for various salient features (namely $B_{P2}\uparrow/B_{P1}\uparrow$, $B_{P2}\downarrow/B_{P1}\downarrow$, $B_{V2}\uparrow/B_{V1}\uparrow$ and $B_{V2}\downarrow/B_{V1}\downarrow$) all depend on (i) and (ii). These are generic features of the model although the detailed variations are dependent on the prescription selected for the background curve and the structure of the peaks of $j_C(B)$.

The model visualizes that after heavy ion irradiation the critical current density $j_C(B)$ remains a continuous function of the flux density but rises smoothly although steeply in the low field range and now exhibits peaks whose summits situated at B_{S1} and B_{S2} on the B axis are linked to the matching field B_ϕ.[6,25-30] For convenience we introduced centrosymmetric triangular peaks instead of more realistic exponential or gaussian peaks. Presumably the width and height of these two peaks is influenced by the random distribution of the columnar defects and an ordered lattice of defects would give rise to higher and narrower peaks.

To reproduce the observed valleys in the relaxation rate versus $B(x)$ we introduce a simple variation of the decay rate along the slopes of the triangular peaks of $j_C(B)$ where the decay rate is smaller by a factor of $\approx 1/2$ at the summits relative to that along their bases. For convenience and in good agreement with observations this factor is chosen the same for both summits. We may conjecture that for a perfectly ordered lattice of columnar defects the decay rate of j_C at the center of the peaks might approach zero.

Our approach provides a good estimate of the dependence of j_C and of its decay rate on the magnetic flux density from the measurements of $M(x)$ and $S(x)$ versus $B(x)$ of Nowak et al[6] and makes detailed predictions regarding the unreported curve of $S(x)$ versus $B(x)$ descending in magnitude. A good fit to the measured curves is obtained by taking the "summit" ratio, $B_{S2}/B_{S1} \approx 2.45$ in the curve of j_C versus B. This is seen to generate the observed "valley" ratio $B_{V2}(x)\uparrow/B_{V1}(x)\uparrow \approx 3$. Future applications of first principle models[30,31] will hopefully account for the appearance of the peaks in the structure of j_C versus B, the variation of the decay rate of j_C along these peaks and the correspondence of these features with B_ϕ and multiples of B_ϕ. Consequently these theoretical efforts should shed light on the physical origin of the ratio $B_{S2}/B_{S1} \approx 2.5$ which emerges from our analysis of the observations of Nowak et al[6].

Appendix

I. Calculation of $B(x)$ profiles.

In our framework where $j_C(B)$ exhibits a peak or peaks four scenarios for the sequences of configurations of flux density profiles (and their "images") need to be envisaged as an increase (decrease) of the magnitude of the applied field H_a induces field shielding (flux retaining) critical current densities in the specimen. These four scenarios are displayed schematically in Fig. A.1. These sketches show the sequences of B profiles for H_a ascending (descending) in magnitude if we regard the surface and the center of a specimen of idealized planar geometry to be situated at $x = 0$ and $x = X$ ($x = X$ and $x = 0$). Note the appearance of a profile labeled 6 (7,8) and the absence of that labeled 2 (4,3) in Fig. A.1b (c,d).

To illustrate the calculation of these sequences of $B(x)$ profiles for $j_{C'}(B)$ displayed in Figs. 2.1 and 3.2 we focus on a representative case namely that labeled 7 in Fig. A.1c. To fix ideas we consider that this profile pertains to the first triangular peak in $j_{C'}(B)$.

For idealized planar geometry Maxwell's eqn., $\nabla \times \bar{B} = \mu_O \bar{j}$, together with the critical state assumption that $j = j_C(B)$, reads,

$$\frac{dB}{dx} = \pm \mu_O j_{C'}(B) \qquad \text{A1}$$

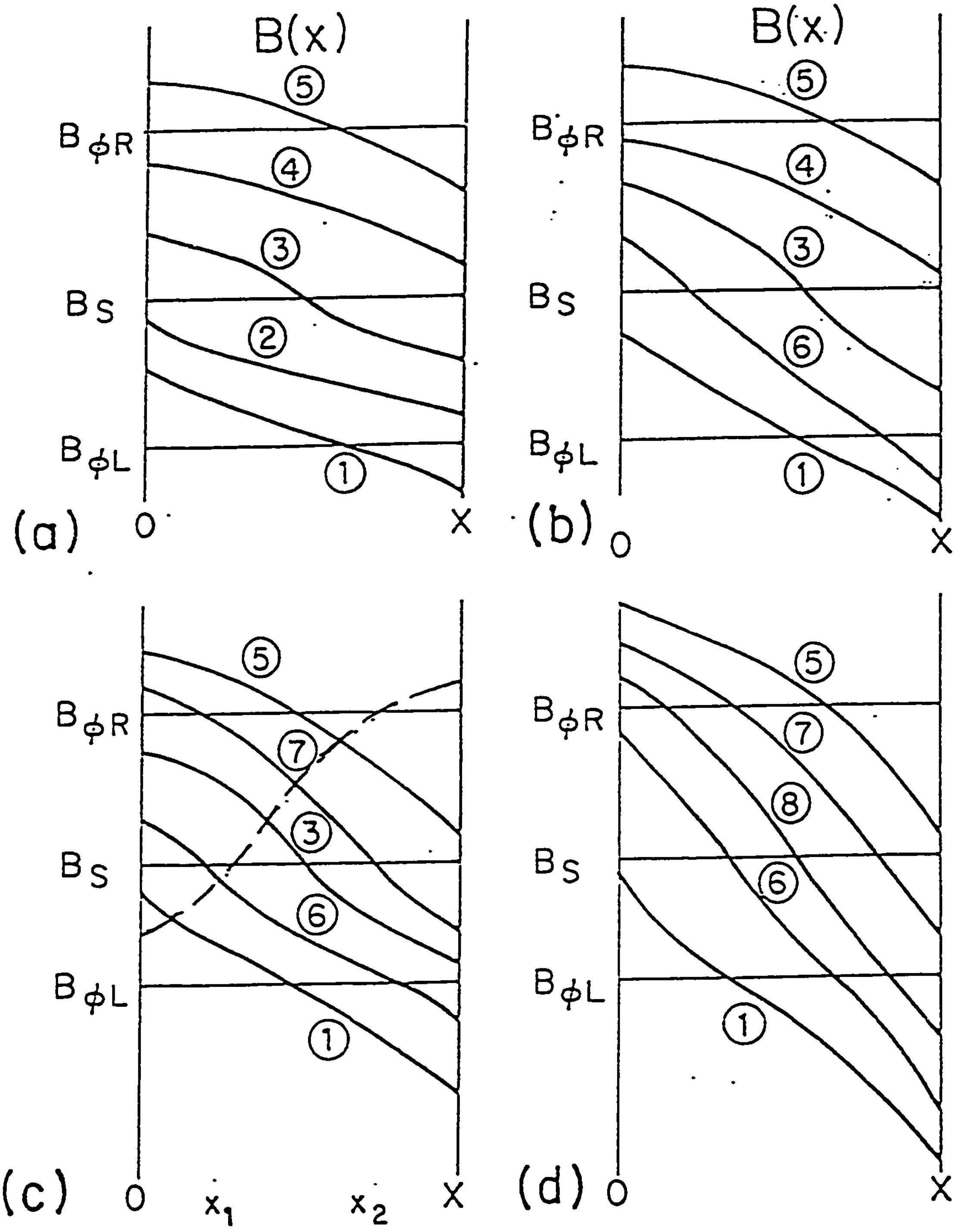

Fig. A.1. Illustrates the four scenarios in the sequences of $B(x)$ profiles which can be encountered as $\mu_0 H_a$ ascending or descending in magnitude generates $B(x)$ profiles traversing a peak in $j_C(B)$. We note that the location of the measuring probe as well as the "structure" of $j_C(B)$ (see Fig. 3.2) prescribing the $B(x)$ profiles determine which scenario is encountered.

First we consider $B(x)$ ascending in magnitude. For the region, $0 \le x \le x_1$, where j_C is given by $j_C = j_O B_{ref}^n / (B + B_O)^n$, (eqn. 3.2), integration of eqn. A1 leads to,

$$B(x) = \{(B_i + B_O)^{n+1} - \mu_O (n+1) j_O B_{ref}^n x\}^{1/(n+1)} - B_O \qquad \text{A2}$$

where $B_i = \mu_O H_a$ is the flux density just inside the surface.

Letting $B(x_1) = B_{\phi 1R}$ gives,

$$x_1 = \frac{(B_i + B_O)^{n+1} - (B_{\phi 1R} + B_O)^{n+1}}{\mu_O (n+1) j_O B_{ref}^n} \qquad \text{A3}$$

For the region, $x_1 \le x \le x_2$, where $j_C = j_{C1R} = j_{S1} \{B_{B1} - B(x)\} / \{B_{B1} - B_{S1}\}$ (eqn. 3.3b), integration of eqn. A1 leads to,

$$B(x) = B_{B1} - (B_{B1} - B_{\phi 1R}) e^{\mu_O j_{S1} (x - x_1)/(B_{B1} - B_{S1})} \qquad \text{A4}$$

Letting $B(x_2) = B_{S1}$, gives,

$$x_2 = \frac{(B_{B1} - B_{S1})}{\mu_O j_{S1}} \ln\left\{\frac{B_{B1} - B_{S1}}{B_{B1} - B_{\phi 1R}}\right\} + x_1 \qquad \text{A5}$$

where x_1 is given by eqn. A3.

For the region, $x_2 \le x \le X$, where $j_C = j_{C1L} = j_{S1} \{B(x) - B_{A1}\} / \{B_{S1} - B_{A1}\}$ (eqn. 3.3a), integration of eqn. A1 leads to,

$$B(x) = B_{A1} + (B_{S1} - B_{A1}) e^{-\mu_O j_{S1} (x - x_2)/(B_{S1} - B_{A1})} \qquad \text{A6}$$

where x_2 is given by eqn. A5.

For H_a descending in magnitude we focus on the $B(x)$ profile shown by the dashed curve, also labeled 7 in Fig. A.1c. The procedure already outlined leads to,

$$B(x) = B_{A1} - (B_i - B_{A1}) e^{\mu_O j_{S1} x / (B_{S1} - B_{A1})} \qquad \text{A7}$$

valid for $0 \le x \le x_1$ where,

$$x_1 = \frac{(B_{S1} - B_{A1})}{\mu_O j_{S1}} \ln\left\{\frac{B_{S1} - B_{A1}}{B_i - B_{A1}}\right\} \qquad \text{A8}$$

and,

$$B(x) = B_{B1} - (B_{B1} - B_{S1}) e^{-\mu_O j_{S1} (x - x_1) / (B_{B1} - B_{S1})} \qquad \text{A9}$$

valid for $x_1 \le x \le x_2$, where x_2 is given by eqn. A5 but where x_1 is now given by eqn. A8. Also,

$$B(x) = \left\{(B_i + B_O)^{n+1} + \mu_O (n+1) j_O B_{ref}^n x\right\}^{1/(n+1)} - B_O \qquad \text{A10}$$

valid for $x_2 \le x \le X$.

The parameters which determine the "background" $j_C(B)$ (eqn. 3.2), namely j_O, B_{ref}, B_O and n are selected to provide a satisfactory description of the observed "background" curve for $|M(x)|$ versus $B(x)$ ascending or descending. The parameters which determine the location, width and height of the triangular peaks in $j_C(B)$, hence $B_{\phi 1L}$, $B_{\phi 1R}$, j_{S1}, $B_{\phi 2L}$, $B_{\phi 2R}$ and j_{S2} are selected to give a good description of the peaks observed for $|M(x)|$ versus $B(x)$ ascending or descending in magnitude.

The requirement that $j_C(B)$ be continuous is met by the conditions that,

$$j_C(B_{\phi 1L}) = j_O\left(\frac{B_{ref}}{B_{\phi 1L} + B_O}\right) = j_{C1L} = j_{S1}\left(\frac{B_{\phi 1L} - B_{A1}}{B_{S1} - B_{A1}}\right) \qquad \text{A11}$$

$$j_C(B_{\phi 1R}) = j_O\left(\frac{B_{ref}}{B_{\phi 1R} + B_O}\right) = j_{C1R} = j_{S1}\left(\frac{B_{B1} - B_{\phi 1R}}{B_{B1} - B_{S1}}\right) \qquad \text{A12}$$

which prescribe the parameters B_{A1} and B_{B1}, and the similar conditions,

$$j_C(B_{\phi 2L}) = j_o\left(\frac{B_{ref}}{B_{\phi 2L} + B_O}\right) = j_{C2L} = j_{S1}\left(\frac{B_{\phi 2L} - B_{A2}}{B_{S2} - B_{A2}}\right) \qquad \text{A13}$$

$$j_C(B_{\phi 2R}) = j_O\left(\frac{B_{ref}}{B_{\phi 2R} + B_O}\right) = j_{C2R} = j_{S2}\left(\frac{B_{B2} - B_{\phi 2R}}{B_{B2} - B_{S2}}\right) \qquad \text{A14}$$

which dictate the parameters B_{A2} and B_{B2}. In order that the triangular peaks be centrosymmetric we write,

$$B_{S1} = (B_{A1} + B_{B1})/2 \qquad \text{and} \qquad B_{S2} = (B_{A2} + B_{B2})/2 . \qquad \text{A15}$$

II. Calculation of relaxation rate $R(x)$

The local relative relaxation rate $R(x)$ is calculated by letting the critical current density parameters j_O, j_{S1} and j_{S2} decay to, $j_O' = j_O - \Delta j_O$, $j_{S1}' = j_{S1} - \Delta j_{S1}$ and $j_{S2}' = j_{S2} - \Delta j_{S2}$ in the expressions for the $B(x)$ profiles. To generate differences in decay rates for $j_C(B)$ along the triangular peaks relative to that prevailing along the background curve we write,

$$\frac{\Delta j_{S1}}{j_{S1}} = f_1 \frac{\Delta j_O}{j_O} \qquad \text{and} \qquad \frac{\Delta j_{S2}}{j_{S2}} = f_2 \frac{\Delta j_O}{j_O} \qquad \text{A16}$$

We also stipulate that, (i) $j_C(B)$ remains continuous as it decays, and, (ii) the boundaries $B_{\phi 1L}$, $B_{\phi 1R}$, $B_{\phi 2L}$ and $B_{\phi 2R}$ as well as the position of the peak centers, B_{S1} and B_{S2}, all remain fixed as illustrated in Fig. 4.1. These conditions then dictate that the relative decay rate of j_C vary linearly versus B along the slopes of the triangular peaks. Stipulations (i) and (ii) prescribe the evolution of the parameters B_{A1}, B_{B1}, B_{A2} and B_{B2} to a new set denoted B'_{A1}, B'_{B1}, B'_{A2} and B'_{B2} via eqns. A11 through A16. We note that the triangular peaks do not remain centrosymmetric as $j_C(B)$ decays since the slope on their left becomes steeper than that on their right (see Fig. 4.1). This feature of our model will however play a role only after appreciable decay has occurred. For the calculations displayed in Figs 4.2 through 4.5 we have focused only on the initial decay rate.

Introducing j_O, j_{S1} and j_{S2} and the corresponding set of parameters, B'_{A1}, B'_{B1}, B'_{A2} and B'_{B2} into the expressions for $B(x)$ (viz. eqns. A2 through A10) for the profile under scrutiny we then calculate,

$$R(x) = \left| \frac{B_f(x) - B(x)}{B_n(\Delta j_O / j_O)} \right| \qquad \text{and} \qquad R_n(x) = R(x) / \left| \mu_O M(x) \right| / B_n$$

for various selected locations of the flux density sensor in the specimen. Here $B_f(x)$ denotes the infinitesimally relaxed profiles.

We note that our results also pertain to infinite cylinder geometry by substituting $(R-r)/R$ for x/X in the expressions for the sequences of $B(x)$ profiles.

References

1. "Critical Currents in Superconductors", A.M. Campbell and J.E. Evetts, Taylor and Francis, 1972
2. "Introduction to Superconductivity", Michael Tinkham, McGraw-Hill, 1975
3. "The Superconducting State", A.D.C. Grassie, Sussex University Press, 1975
4. "Introduction to High-Temperature Superconductivity", Thomas P. Sheahen, Plenum Press, 1995
5. "The New Superconductors", Frank J. Owens and Charles P. Poole Jr., Plenum Press, 1996
6. E.R. Nowak, S. Anders, H.M. Jaeger, J.A. Fendrich, W.K. Kwok, R. Mogilevsky and D.G. Hinks, Phys. Rev. B 54, R12725 (1996)
7. K.M. Beauchamp, T.F. Rosenbaum, U. Welp, G.W. Crabtree and V.M. Vinokur, Phys. Rev. Lett. 75, 3942 (1995)
8. K.M. Beauchamp, L. Radzihovsky, E. Shung, T.F. Rosenbaum, U. Welp and G.W. Crabtree, Phys. Rev. B52, 13025 (1995)
9. M.A.R. LeBlanc, Daniel S.M. Cameron and David LeBlanc, Phys. Rev. B55, R6141 (1997)
10. L. Radzihovsky, Phys. Rev. Lett. 74, 4919 (1995)
11. Y.B. Kim, C.F. Hempstead, and A.R. Strnad, Phys. Rev. Lett. 9, 306 (1962); Phys. Rev. 129, 528 (1963); 131, 2486 (1963)
12. L. Civale, A.D. Marwick, T.K. Worthington, M.A. Kirk, J.R. Thompson, L. Krusin-Elbaum, Y. Sun, J.R. Clem and F. Holtzberg, Phys. Rev. Lett. 67, 648 (1991)

13. W. Gerhauser, G. Ries, H.W. Neumuller, W. Schmidt, O. Eibl, G. Saemann-Ischenko and S. Klaumunzer. Phys. Rev. Lett. 68, 879 (1992)

14. R.C. Budhani, M. Suenaga and S.H. Liou, Phys. Rev. Lett. 69, 3816 (1992)

15. L. Krusin-Elbaum, L. Civale, J.R. Thompson and C. Feild, Phys. Rev. B53, 11744 (1996)

16. M. Konczykowski, F. Rullier-Albenque, E.R. Yacoby, A. Shaulov, Y. Yeshurun and P. Lejay, Phys. Rev. B44, 7167 (1991)

17. M. Konczykowski, V.M. Vinokur, F. Rullier-Albenque, , Y. Yeshurun and F. Holtzberg, Phys. Rev. B47, 5531 (1993)

18. M. Konczykowski, D. Majer, E. Zeldov, N. Chikumoto and V.M. Vinokur, Physica C235-240, 2965 (1994)

19. M. Konczykowski, N. Chikumoto, V.M. Vinokur and M.V. Feigelman, Phys. Rev. B51, 3957 (1995)

20. C.J. van der Beek, M. Konczykowski, V.M. Vinokur, G.W. Crabtree, T.W. Li and P.H. Kes, Phys. Rev. B51, 15492 (1995)

21. Y. Yeshurun, A.P. Malozemoff, F. Holtzberg and T.R. Dinger, Phys. Rev. B38

22. Donglu Shi, Ming Xu, A. Umezawa and Ronald F. Fox, Phys. Rev. B42 2062 (1990)

23. Ming Xu, Donglu Shi, A. Umezawa, K.G. Vanderwoort and G.W. Crabtree, Phys. Rev. B43, 13049 (1991)

24. Yang Ren Sun, J.R. Thompson, D.K. Christen, F. Holtzberg, A.D. Marwick and J.G. Ossendon, Physica C194, 403 (1992)

25. A.N. Lykov, Sol. St. Comm. 86, 531 (1993)

26. V.V. Metlushko, M. Baert, R. Jonckheere, V.V. Moshchalkov and Y. Bruynseraede, Sol. St. Comm. 91, 331 (1994)

IMAGE EVALUATION
TEST TARGET (QA-3)

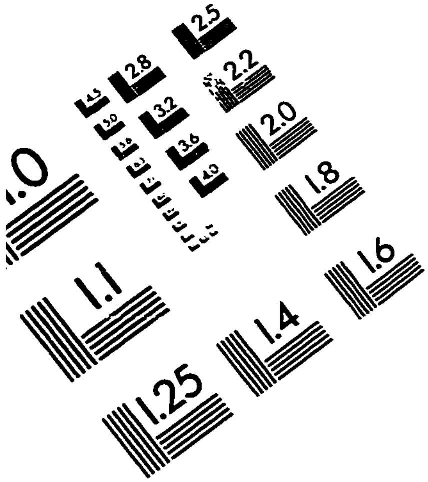

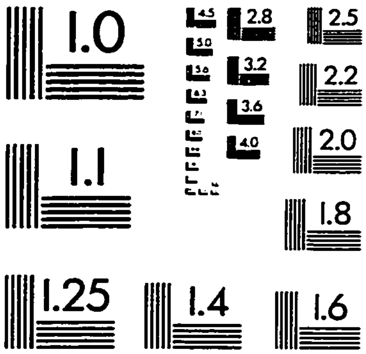

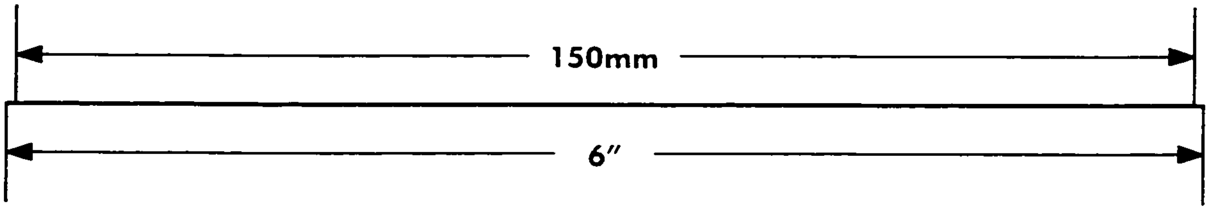

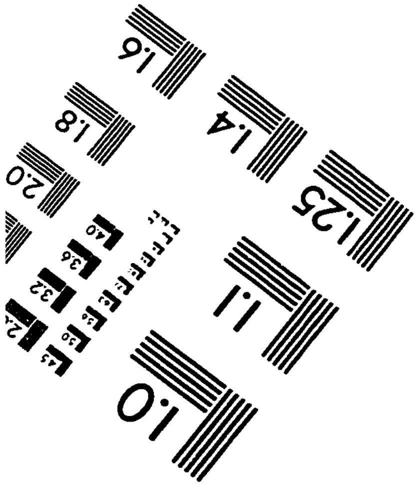

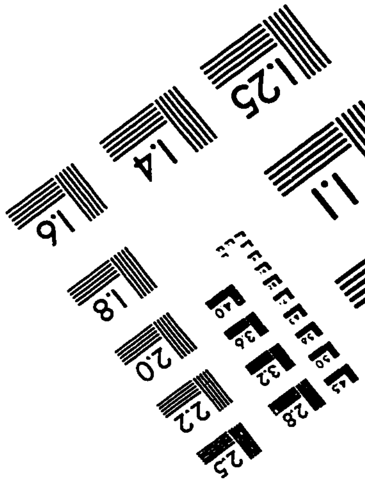

APPLIED IMAGE . Inc
1653 East Main Street
Rochester, NY 14609 USA
Phone. 716/482-0300
Fax: 716/288-5989